REVIEW

Synthetic strategies to nanostructured photocatalysts for CO_2 reduction to solar fuels and chemicals

Donna Chen,[a] Xingguang Zhang[b] and Adam F. Lee*[b]

Artificial photosynthesis represents one of the great scientific challenges of the 21st century, offering the possibility of clean energy through water photolysis and renewable chemicals through CO_2 utilisation as a sustainable feedstock. Catalysis will undoubtedly play a key role in delivering technologies able to meet these goals, mediating solar energy *via* excited generate charge carriers to selectively activate molecular bonds under ambient conditions. This review describes recent synthetic approaches adopted to engineer nanostructured photocatalytic materials for efficient light harnessing, charge separation and the photoreduction of CO_2 to higher hydrocarbons such as methane, methanol and even olefins.

1. Introduction

The use of sunlight to split water as a source of electrons that can be stored in chemical bonds for the production of primary energy carriers and molecular building blocks underpins the natural world. Humanity remains highly dependent upon such elegant photosynthetic processes, developed through natural evolutionary selection, for the sustainable growth of biomass, which literally feeds our planet. However, recent technological breakthroughs offer a glimpse of a mid-term future in which anthropogenic systems will enable artificial photosynthesis with efficiencies surpassing that of plants, to deliver solar fuels and chemicals.[1,2] Arguments for the development and global deployment of artificial photosynthesis technology to reduce anthropogenic CO_2 emissions from their historic high,[3,4] increase fuel security,[5] and support a sustainable global economy and ecosystem have been recently expounded,[6,7] and new mechanisms for enhancing the policy and governance profile in the context of energy sustainability sought.

Solar fuels include H_2 (from the reduction of H^+ derived from water photolysis) or carbon-based fuels (derived from the photoreduction of CO_2) such as methane, methanol or CO, and

[a]School of Chemistry, Cardiff University, Cardiff, UK
[b]European Bioenergy Research Institute, Aston University, Birmingham, UK. E-mail: A.F.Lee@aston.ac.uk; Tel: +44 (0)121 2044036

Donna Hui Lin Chen relocated to Sydney, Australia, in 2003 for her BSc degree, majoring in Nanotechnology, at The University of New South Wales. She subsequently moved to the University of Sydney where she commenced a PhD at the School of Chemistry focusing on the synthesis, characterisation, testing and study of potential visible light active catalysts for H_2 generation. In 2012, she took up a Research Assistant position at Cardiff University, where she initiated a CO_2 photoreduction project. She is interested in technologies that minimise the environmental impact of industrial processes.

Xingguang Zhang received his Bachelor of Engineering in Chemical Engineering and Technology from Guizhou University (Guiyang, China) in 2007, Master of Engineering in Industrial Catalysis under the supervison of Professor Jun Wang in Nanjing Tech University (Nanjing, China) in 2010, and PhD under the supervision of Dr Xuebin Ke and Professor Huaiyong Zhu at Queensland University of Technology (Brisbane, Australia) in 2014. He is currently a research associate working with Professor Adam Lee and Professor Karen Wilson to develop supported metal catalysts and solid acid catalysts for clean chemicals synthesis within Aston University and UK Catalysis Hub.

This journal is © The Royal Society of Chemistry 2015

J. Mater. Chem. A, 2015, **3**, 14487–14516 | 14487

associated higher hydrocarbons *via* subsequent well-established industrial thermal chemistry. Artificial photosynthesis may be considered to span the genetic engineering of plant or algal crops to tailor their lignocellulosic or lipid constituents for biofuels production, synthetic biology to combine incorporate cyanobacterial proteins into chloroplasts and hence improve the rate of CO_2 fixation,[8] and the use of nanotechnology *via* inorganic or molecular systems to produce photo-electrochemical devices.[9–12] In contrast to a number of competing renewable energy technologies, such as wind, tidal and photovoltaics, wherein electricity is the end product, and hence a dependency exists upon concomitant advances in storage and smart grid capabilities, the trapping of solar energy within chemical bonds provides immediate access to (potentially high) energy density carriers for transportation fuels. Water photooxidation for H_2 production has been reviewed extensively elsewhere;[13–15] hence this review focuses on photocatalytic CO_2 reduction.

The potential of CO_2 as a chemical feedstock *via* chemical and biochemical,[16] electrocatalytic[17,18] and photocatalytic transformations has been widely recognised, with methane[19] and methanol[20–23] obvious targets to replace fossil fuels in stationary power generation and transportation. Another key area in which CO_2 sequestration may have a profound impact is as a carbon source for renewable polymers and plastics and solvent.[24–26] In the context of polymers, the thermochemical incorporation of CO_2 into polycarbonates/carbamates is well-established; however, its direct photoreduction to light (C_1–C_3) olefins represents a greater challenge. Olefins and their polymers are the single largest chemical commodity in the world, with annual global ethene and propene production capacity in 2012 around 156 and 80 Mt respectively.[25,27] These olefins are currently obtained from non-renewable fossil fuels:[28] commercial ethene and propene manufacture involves steam or catalytic cracking of naphtha, gasoil and condensates to hydrocarbon mixtures followed by distillation. Cracking crude

oil to produce ethene or propene is thermodynamically unfavourable ($\Delta G \approx +100$ kJ mol^{-1}), requiring high temperatures (>600 °C) to overcome the huge activation barriers to C–C cleavage (280 kJ mol^{-1} for kerosene conversion[29]). Hence steam cracking is the most energy-consuming process in chemistry, accounting for 8% of the sector's primary energy use and annual CO_2 emissions of 180–200 Mt.[28]

1.1. Brief history and fundamental principles of photocatalytic materials for CO_2 reduction

Renewable solar energy, harnessed *via* innovative catalysts and reactors, has the potential to photoreduce linear CO_2 molecules by breaking the C=O bonds to form C–H bonds and then to yield products, such as methane, methanol or light olefins (*e.g.* $CO_2 + 2H_2O \leftrightarrow CH_3OH + 3/2O_2$; $CO_2 + 2H_2O \leftrightarrow CH_4 + 2O_2$; and $2CO_2 + 2H_2O \leftrightarrow C_2H_4 + 3O_2$), thereby creating new chemical supply chains free of current dependencies on oil, coal and natural gas and offering an economical and potentially environmentally-benign CO_2 utilisation process (Fig. 1).[30]

Great challenges lie in the robust chemical state of carbon atoms in CO_2, which requires not only the participation of incident protons but also effective excited electrons, and thus additional reductive agents can offer better opportunities to facilitate the activation of CO_2. In this regard, H_2O is preferred as a reducing agent because it simultaneously takes advantage of water oxidation and CO_2 fixation compared with other sacrificing reductive agents such as amines, H_2, and S^{2-}. Hence, the harvesting of input energy by means of photocatalytic materials from incident light plays a pivotal role in achieving these processes. The first study on the photocatalytic CO_2 reduction was reported by Halmann in 1978, employing a Hg lamp and single crystal, p-type GaP cathode within an electrochemical cell through which CO_2 was bubbled to yield formic acid, formaldehyde and methanol.[31] A year later, Inoue and coworkers reported the photoelectrocatalytic reduction of CO_2 to formic acid, formaldehyde, methanol and methane, over a variety of semiconductors including TiO_2, ZnO, CdS, GaP, SiC, and WO_3.[32]

These pioneering studies were followed by the development of visible-light driven photocatalysts and production of more

Adam Lee is Professor of Sustainable Chemistry and an EPSRC Leadership Fellow in the European Bioenergy Research Institute, Aston University. He holds a BA and PhD from the University of Cambridge, and following Lecturer/Senior Lecturer roles at the Universities of Hull and York respectively, has held Chair appointments at Cardiff, Warwick and Monash universities. His research addresses the rational design of nanoengineered materials for clean catalytic technologies, notably sustainable chemical synthesis and energy production, and the development of in situ methods providing molecular insight into surface reactions, for which he was awarded the 2012 Beilby Medal and Prize by the Royal Society of Chemistry.
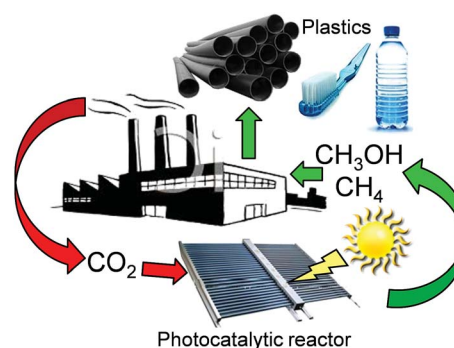

Fig. 1 Schematic of a carbon zero route to solar fuels and renewable olefins through the photocatalytic reduction of CO_2.

14488 | *J. Mater. Chem. A*, 2015, **3**, 14487–14516

This journal is © The Royal Society of Chemistry 2015

functionalised organic moieties, *e.g.* CO_2 photoreduction *via* colloidal CdS aqueous solutions to glyoxylic and acetic acids.[33]

Moreover, large-scale photocatalytic CO_2 reduction to solar fuels or chemicals requires intensified processing and carefully engineered robust (and hence likely heterogeneous) catalysts with high accessibility, able to activate small molecules at ambient conditions.[34] This challenge can only be met through novel nanotechnologies, which permit the construction of tailored materials whose structure (and function) can be precisely tuned.[35–37] A practical photocatalytic chemical reactor requires appropriately selected coupled redox reactions, and the ability to efficiently harness light capable of driving the requisite electron-transfer chemistry.[38] The former favours water as a green chemical reductant (mimicking natural photosynthesis), while the latter requires active catalysts either able to absorb solar energy directly or coupled to sensitisers which help gather and focus energy onto the active sites.

The optical properties of potential solid photocatalysts are dictated by the rate-limiting oxidation and reduction steps that must occur at the surface of their nanostructures:[39] $2H_2O \rightarrow O_2 + 4H^+ + 4e^-$; $CO_2 + e^- \rightarrow CO_2^{\cdot-}$ (E^o_{redox} = +1.64 V and −1.90 V, respectively, on the basis of NHE (normal hydrogen electrode) at pH = 7). Such values impose a minimum for the photoexcitation energy of electrons needed to reduce CO_2, whereas few pure materials are photoresponsive to these wavelengths and catalytically active towards CO_2 and water conversion, even though visible light can create sufficiently excited electrons. These insurmountable limitations necessitate the development of new photocatalytic materials particularly with specially-nanostructured antennas to harvest both UV and visible light efficiently and to initiate the chemical reactions effectively.

1.2. Strengths and challenges of nanostructured photocatalysts

Nanoscale materials often exhibit unique physicochemical which diverge widely from their bulk counterparts. Such nanomaterials, commonly synthesised in the form of nanoparticles (NPs), nanofibres (NFs) and nanotubes (NTs), in addition to more exotic topologies such as nanobelts and nanoflowers, afford high surface areas, tunable architectures and distinct electronic surface states. In particular, photocatalytic nanostructures can offer high densities of photoactive surface sites and thin-walled structures/ultrathin films able to facilitate rapid interfacial charge carrier transport to adsorbates.[35,40] For many years, CO_2 reduction has centred around titania-based photocatalysts, which are only able to utilise a fraction of the solar spectrum (∼2%, mainly as UVA),[41–45] and require exploitation of quantum effects or doping to reduce their intrinsic band gaps,[46] sometimes in combination with inorganic or organic supramolecular (biomimetic) sensitisers.[47] Significant advances in artificial photosynthesis have been achieved through such photocatalytic nanoarchitectures,[37,48] *e.g.* the discovery of 'self-repairing' Co_xPO_4 catalysts producing O_2 akin to the natural Mn catalyst in photosystem II,[49] corrosion resistant TiO_2 nanocomposites able to split water[50] or reduce CO_2 with H_2O to yield CH_4 and olefins,[40,51] and the use of metal

oxynitrides[52] and polymeric nitrides[53] for efficient water splitting under visible light. Solar CH_4 production from CO_2 has seen dramatic improvements in recent years, with TiO_2 NTs delivering 17.5 nanomoles h^{-1} cm^{-2} mW^{-1} of hydrocarbons from 1 bar CO_2 under sunlight, with a quantum efficiency of 0.74%,[40] defined throughout this review as:

$$\eta = \frac{\Sigma_i M_i n_i}{P_m}$$

where M_i is the mols of product i, n_i is the number of electrons attending the production of product i, and P_m is mols of incident photons.[54,55] Cu-doped titania coatings deposited on a monolithic substrate have even been reported able to deliver 117 nanomoles h^{-1} cm^{-2} $m W^{-1}$ of methane.[56] In addition to maximising the quantum efficiency, productivity and selectivity towards hydrocarbons, the stability of semiconductor photocatalysts under reaction conditions (notably resistance to photocorrosion[57,58]) and routes to their incorporation into reactor designs which facilitate efficient light absorption and mass transport,[59–61] are also key considerations.

Significant developments in molecular nanocatalysts for photochemical CO_2 reduction have been achieved and reviewed;[38,62,63] nevertheless, improvements in the mechanical strength, physicochemical stability and photocatalytic efficiency of such materials remain necessary to meet the engineering requirements for large-scale applications. Molecular band structures control incident light absorption, electron–hole pair generation and charge carrier migration. Similarly, energy band engineering of semiconductor photocatalysts to impede the recombination of photo-excited electron–hole pairs and enhance light absorption is of paramount importance.[64–66] A further challenge is the optimisation of CO_2 and H_2O adsorption over photocatalyst surfaces, which is poorly understood to date,[67,68] and requires a thorough knowledge of the atomic structure of the photocatalyst interface. Advanced inorganic synthetic methods afford precise manipulation of exposed crystal facets, morphologies, structural periodicity, and hierarchical pore networks,[69–71] in addition to the co-assembly of sensitisers or co-catalysts and promoters. Meeting these challenges will also necessitate continued advances in our fundamental understanding of photocatalytic reaction and deactivation mechanisms. This review discusses progress in the design of nanostructured solid materials CO_2 to solar fuels and chemicals, with a particular focus on new synthetic routes to inorganic photocatalysts possessing well-defined physichochemical properties and the elucidation of associated structure-function relations. Materials chemistry approaches to porous and layered semiconductor architectures, and hybrid photoactive nanomaterials (*e.g.* plasmonic nanostructures) are also highlighted, and the most active and selective systems benchmarked.

1.3. Mechanistic complications in CO_2 photoreduction

Before considering the vast array of nanomaterials employed in for CO_2 photoreduction, we consider briefly some of the particular analytical challenges in evaluating photoactivity and

This journal is © The Royal Society of Chemistry 2015

J. Mater. Chem. A, 2015, **3**, 14487–14516 | **14489**

product formation. Carbon-containing precursors and/or solvents are employed in the synthesis of most heterogeneous photocatalysts, and few studies quantify the carbon content of the resulting as-prepared materials. Such carbonaceous residues can either decompose directly upon subsequent irradiation,[68] or react with photoexcited molecular species generated from CO_2 or water,[72] to liberate carbon-containing liquid/gas phase products. Discriminating whether such products originate *solely* from desired CO_2 conversion and/or carbon residues is not possible by conventional chromatographic methods, and rarely accorded the attention deserved.

Yui and co-workers reported that organic adsorbates such as acetic acid present over commercial, untreated P25 TiO_2 were responsible for CH_4 evolution as a major product during CO_2 photoreduction.[68] A photo-Kolbe decaboxylation mechanism was proposed that accounted for the observed methane solely in terms of acetic acid reduction: $CH_3COOH + H^+ \rightarrow CH_3^{\cdot} + CO_2 + H^+$; $CH_3^{\cdot} + CH_3COOH \rightarrow CH_2COOH^{\cdot} + CH_4$. Pre-calcination and washing of the TiO_2 suppressed methane production, with CO the dominant products; convincing evidence for the Kolbe mechanism hypothesised. Isotopic-labelling using $^{13}CO_2$ over an organic-free 2 wt% Pd/TiO_2 catalyst revealed the co-production of $^{13}CH_4$ (unequivocally through direct photoreduction) and some $^{12}CH_4$ likely originating from the CO_3^{2-} species on the parent titania. In a complementary investigation, Yang *et al.* explored the mechanism of $^{13}CO_2$ photoreduction in H_2O over $Cu(I)/TiO_2$ by means of *in situ* DRIFT spectroscopy.[72] ^{12}CO was identified from its 2115 cm^{-1} $Cu(I)$–CO signature as the primary product of reaction between photocatalytically activated adsorbed water and carbonaceous residues on the as-prepared photocatalyst surface. The residual surface carbon reflects the use of a titanium(IV) butoxide precursor and polyethylene glycol structure-directing agent, with (an unquantified amount of) carbon persisting even after the resulting sol–gel was calcined at 500 °C for 5 h. Prolonged UV irradiation of the fresh catalyst under moist air to remove carbon contaminants significantly lowered the yield of reactively-formed CO, although some ^{13}CO was observed, evidencing true CO_2 photoreduction. These studies highlight the importance of eliminating organic (and carbonate) surface residues from photocatalysts prior to CO_2 photoreduction tests, *via e.g.* high temperature calcination, solvent washing and/or pre-exposure to UV light in the absence of CO_2. Yang and co-workers also recommended that an additional control experiment be undertaken to ensure no carbon-containing products are formed in the absence of CO_2 but presence of H_2O. To date very few studies have acted upon this sound recommendation.

The overwhelming majority of CO_2 photoreduction employs water as the electron (net hydrogen) source, and should therefore be accompanied by oxygen co-generation. Selective reduction to CO should proceed according to: $CO_2 + 3H_2O \rightarrow CO + 3H_2 + 2O_2$ (combining $2H_2O \rightarrow 2H_2 + O_2$ and $CO_2 + H_2O \rightarrow CO + H_2 + O_2$), for which the molar ratio of $(H_2 + CO) : O_2$ should be 2 : 1. However, very few studies report such oxygen evolution, let alone endeavour to quantify it and thereby demonstrate that water is the sole electron donor. In the case of ZrO_2 in aqueous $NaHCO_3$,[73] $KTaO_3$ (ref. 74) and Ag doped $ALa_4Ti_4O_{15}$ (A = Ca, Sr,

and Ba) perovskites,[75] the co-evolution of CO, H_2 and O_2 is reported with the predicted 2 : 1 stoichiometry; albeit isotopic labelling experiments with $^{13}CO_2$ also revealed the formation of trace ^{12}CO over for $KTaO_3$ due to either $^{12}CO_2$ from reactor purging or organic residues within the photoreactor. Isotope labelling, a full complement of control experiments, and careful analysis of evolved oxygen are thus critical to accurately quantify CO_2 photoreduction and understand underlying reaction pathways.

2. Developments in nanostructured materials

2.1. Crystallinity and the role of engineered surface defects

The catalytic behaviour of photocatalysts is intrinsically linked to their surface electronic/optical properties and adsorption behaviour, all of which can (in principle) be systematically tuned through crystal structure engineering; the nature, dimensions, uniformity and termination of crystalline phases strongly influence their resultant photocatalytic efficiency.[76] For instance, monoclinic sheet-like $BiVO_4$ significantly outperformed tetragonal rod-like $BiVO_4$ counterparts in the rate of CO_2 photoreduction to C_2H_5OH (accompanied by O_2 evolution), under both UV and visible light illumination in the presence of water.[77] These monoclinic and tetragonal phases were obtained by introducing CTAB (cetyltrimethyl ammonium bromide) or PEG (polyethylene glycol), respectively, during $BiVO_4$ synthesis. The superior photoactivity of the monoclinic $BiVO_4$ was attributed to the more asymmetric local environment of the Bi^{3+} ions relative to those within the tetragonal phase. Accordingly, the Bi^{3+} ions exhibit stronger lone pair character in the monoclinic phase and are hence drive to form Bi–O bonds with CO_2 bound as the carbonate, and consequential transfer of photogenerated electrons from the V 3d bands into the chemisorbed CO_3^{2-}. It is worth noting that these two phases exhibited different UV-Vis absorbances, with the band gaps of monoclinic and tetragonal $BiVO_4$ around 2.24 eV and 2.56 eV respectively. More recently, Li *et al.* demonstrated that cubic $NaNbO_3$ was more effective than orthorhombic $NaNbO_3$ for CO_2 photoreduction.[78] The cubic $NaNbO_3$ (c-$NaNbO_3$), which is normally only stable at $T > 813$ K, was successfully prepared through a furfural alcohol derived polymerisation-oxidation (FAPO) method in the presence of P123 as a surfactant stabiliser. The more common orthorhombic $NaNbO_3$ (o-$NaNbO_3$) phase was prepared through a polymerised complex (PC) method. While c-$NaNbO_3$ comprised predominantly cuboid morphologies, a mixture of irregular and cuboid particles was obtained for o-$NaNbO_3$. Both crystal phases exhibited a comparable crystallite size (c-$NaNbO_3$ = 18.5 nm *versus* o-$NaNbO_3$ = 23.1 nm) and surface area (c-$NaNbO_3$ = 28.6 $m^2 g^{-1}$ *versus* o-$NaNbO_3$ = 26.4 $m^2 g^{-1}$), however, the band gap of c-$NaNbO_3$ (3.29 eV) was smaller than that of o-$NaNbO_3$ (3.45 eV). Under UV irradiation (300 W Xe arc lamp) in the presence of a Pt co-catalyst and water vapour, c-$NaNbO_3$ generated almost double the amount of CH_4 (0.486 μmol h^{-1}) than that obtained from o-$NaNbO_3$ (0.245 μmol h^{-1}) in a gaseous, closed circulation system pressurised with 80 kPa CO_2. Density functional

14490 | *J. Mater. Chem. A*, 2015, **3**, 14487–14516

This journal is © The Royal Society of Chemistry 2015

theory (DFT) calculations ascribed this variation in photo-catalytic performance to differences in conduction band (CB) energies, reflecting different octahedral ligand fields. Accordingly, electron excitation and transfer was more efficient over the high symmetry c-NaNbO$_3$ phase than o-NaNbO$_3$. In addition to CO (0.082 μmol h^{-1}) and H$_2$ (0.71 μmol h^{-1}), trace amounts of C$_2$H$_4$, C$_2$H$_6$ and C$_3$H$_8$ were detected during CO$_2$ photocatalysis over the c-NaNbO$_3$.

Numerous preparative routes have been developed to nano-materials with controllable crystal facets such as pH regulation of the synthetic media, or post-synthesis treatments. Truong *et al.* selectively prepared anatase (pH 2, only 3% rutile), rutile (pH 6, only 6% of anatase) and a bi-crystalline anatase(73%)-brookite(27%) composite at pH 10.[79] Under UV (500 W Xe lamp) or visible light irradiation (NaNO$_2$ solution as a UV cut-off filter), and in the presence of a NaHCO$_3$ solution, these materials were able to photoreduce CO$_2$ to CH$_3$OH, whereby the photoactivity followed the order anatase-brookite composite > rutile > anatase > commercial P25. Liu *et al.* also successfully prepared three different nanostructures of TiO$_2$ polymorphs including anatase (TiA) NPs, rutile (TiR) nanoellipses and brookite (TiB) nanorods for CO$_2$ photoreduction,[80] by subjecting the as-synthesised titania to heat treatment under a He environment at 220 °C for 1.5 h to induce surface defects, such as oxygen vacancies (V_O) and Ti^{3+} ions on these TiO$_2$ polymorphs. Illumination by a 150 W solar simulator in the presence of CO$_2$/water vapour revealed the untreated TiO$_2$ polymorphs as active for CO$_2$ photoreduction to CO and a small amount of CH$_4$ under continuous-flow (2.0 mL min^{-1}). Product yields decreased in the order TiA > TiB > TiR. As depicted in Fig. 2, He-treated materials TiA(He) and TiB(He) significantly outperformed their untreated counter-parts, with TiB(He) exhibiting the highest photoactivity, followed by TiA(He); such annealing treatments had less impact upon the photoactivity of TiR wherein the activation barrier to surface oxygen vacancy creation was presumably higher.

In situ DRIFTS and DRUVS suggested that the relative V_O: Ti^{3+} concentration in TiA(He) was comparable to that of TiB(He), while the surface defect concentration on TiR(He) was negligible. The higher photoactivity of TiB(He) and TiA(He) was thus attributed to surface defects, with the energy of vacancy formation for TiB (He) of 5.52 eV lower than that for anatase (5.58 eV) and rutile (5.82 eV). CO$_2$ photoreduction over titania is clearly a strong function of the crystal structure and surface defect density; the latter postulated the active catalytic sites.

An increasing volume of research has established the influence of crystal facets upon photocatalysis; physical and chemical properties of single crystals are highly sensitive to crystallographic termination.[76,81] Calculations have established that the average surface energies of low-index anatase facets decrease in the order 0.90 J m^{-2} (001) > 0.53 J m^{-2} (100) > 0.44 J m^{-2} for (101).[82,83] The highest energy (001) surface is expected to be the most reactive, and indeed experimental studies confirm that dissociative molecular adsorption of water and methanol occur readily on the (001) surface.[84,85] Consequently, efforts to control the morphology of TiO$_2$ have focused on the synthesis of nanostructures preferentially exposing (001) facets or coexposing (001) and (101) facets[86] to enhance water splitting and dye
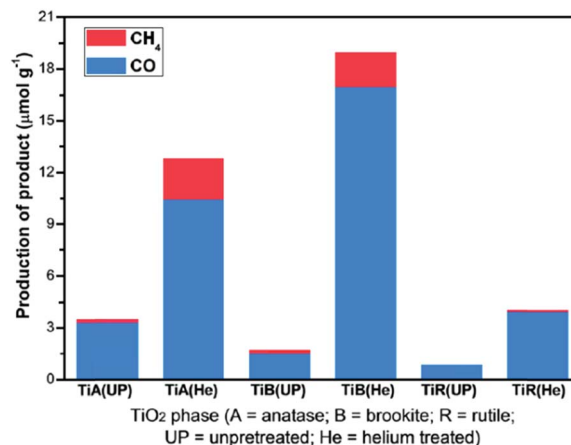

Fig. 2 CH$_4$ and CO productivity from untreated and He-treated TiO$_2$ polymorphs during 6 h illumination under 150 W solar simulator in the presence of CO$_2$/H$_2$O vapour, in a continuous-flow mode photo-reactor operating at a flow rate of 2 mL min^{-1}. Reprinted with permission from ref. 80. Copyright 2012 American Chemical Society.

degradation.[87–90] However, other studies suggest that photore-duction and photooxidation activities follow the order (001) < (101) < (010),[91] with the superior performance of the (010) facet attributed to a synergy between the surface atomic structure (dictating adsorption/reactivity) and electronic band structure (dictating the CB potential).

TiO$_2$ nanorods preferentially exposing (010) facets were therefore screened in CO$_2$ photoreduction.[91] Such nanorods were synthesised by hydrothermal treatment of a H$_{0.68}$Ti$_{1.83}$O$_3$ precursor in the presence of Cs$_2$CO$_3$ as a pH mediator, and subsequent promotion by 1 wt% Pt. The resulting Pt-doped TiO$_2$ nanorods outperformed P25 in CO$_2$ photoreduction by water vapour to CH$_4$ under 300 W Xe lamp UV irradiation in a Teflon-lined steel chamber under 0.06 MPa CO$_2$. Enhanced activity was attributed to the unique properties of (010) facets which promote CO$_2$ adsorption,[92] specifically their more negative conduction band potential. The same group prepared hollow anatase TiO$_2$ single crystals and mesocrystals, wherein both nanostructures were dominated by (101) facets.[93] These materials were successfully synthesised by hydrothermal treatment of a Ti(SO$_4$)$_2$, Na$_3$PO$_4$ and HF solution. Fig. 3A–D shows the resulting 400 nm diameter octahedral single crystals obtained using 500 mM HF; lowering the HF concentration to 400 mM yielded hollow crystals with less prominent octahedral shapes of ~160 nm (Fig. 3B and E). Fig. 3H reveals that these hollow crystals were single crystalline and principally (101) oriented, with a small proportion of higher-index (103) facets. Even lower HF concentrations favoured sphere-like hollow cages 150 nm diameter (Fig. 3C and F), each formed from ~35 nm octahedral crystals, which spontaneously self-organised during crystal growth to adopt a common crystallographic orientation, resulting in 'single crystal-like' mesocrystals with well-defined selected area electron diffraction (SAED) patterns. Under UV irradiation (300 W Xe lamp) and in the presence of a RuO$_2$ co-catalyst and water vapour, the hollow single crystal and mesocrystal materials titanias outperformed a non-porous

This journal is © The Royal Society of Chemistry 2015

J. Mater. Chem. A, 2015, **3**, 14487–14516 | **14491**

single crystal by a factor of 4–5 times in photoreducing CO_2 to CH_4, attributed to their (i) higher surface areas (35 m^2 g^{-1} and 42 m^2 g^{-1} respectively) relative to the solid crystal (17 m^2 g^{-1}) and (ii) shorter diffusion length of charge carriers and concomitant suppressed bulk recombination. Fig. 3J illustrates the different electronic band structures of the single crystal, hollow single crystal and hollow mesocrystal titanias, and more negative CB potential of the hollow mesocrystal.

Adsorbate-induced restructuring of highly reactive facets remains an intrinsic problem due to their high surface energies. In this regard, reagents such HF and isopropanol have been employed as structure-directing agents to favour exposure of (001) facets over single-crystal anatase nanosheets.[60] Use of such capping agents is itself problematic since they must be removed by thermochemical treatment prior to photocatalytic application (*e.g.* solvent extraction or calcination) which in turn may induce surface restructuring/phase changes. Fabrication of stable and uniform nanostructures terminating in specific atomic rearrangements requires continued development.
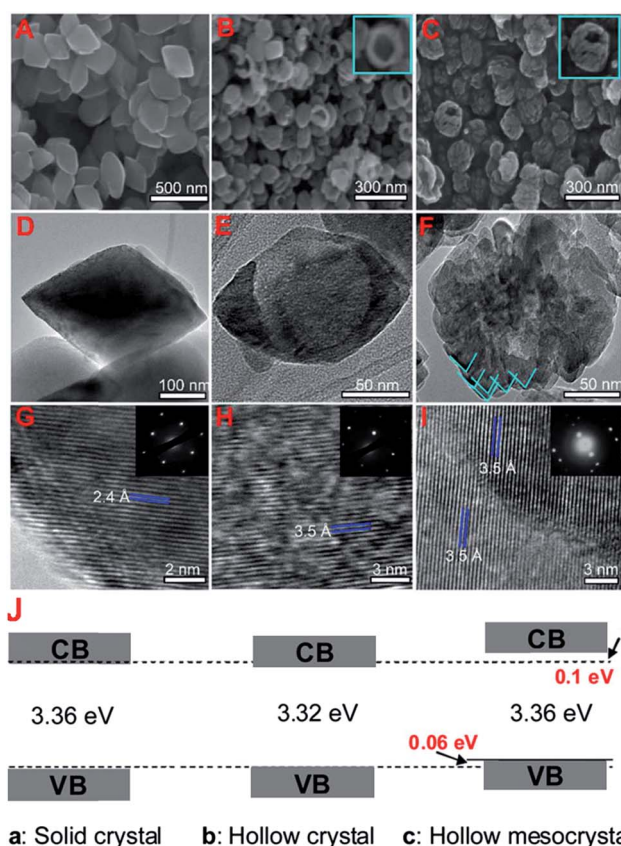

Fig. 3 SEM images (A)–(C), TEM images (D)–(F), HRTEM images (G)–(I) and (J) electronic band structures based on UV-Vis and valence band XPS spectra of single crystal solid anatase TiO_2, single crystal hollow anatase TiO_2, and hollow anatase TiO_2 mesocrystals. Insets in (B) and (C) highlight hollow cores in the single and mesocrystal particles, insets in (G)–(I) show SAED patterns for the solid single crystal, hollow single crystal and mesocrystal anatase TiO_2. Reprinted with permission from ref. 93. Copyright 2012 American Chemical Society.

2.2. Nanostructured photocatalysts

2.2.1. Low dimension nanomaterials. One-dimensional nanomaterials are generally more attractive than their bulk and nanoparticle counterparts in photocatalysis, because they facilitate more efficient electron transport and exhibit higher surface area to bulk volume ratios.[65] Recent work has shown that Zn_2GeO_4 nanoribbons and nanorods photoreduce CO_2 more efficiently than Zn_2GeO_4 prepared through conventional reaction[96,97] As depicted in Fig. 4a, single crystalline Zn_2GeO_4 nanoribbons of around 7 nm in thickness, 20–50 nm width and hundreds of microns long, were successfully prepared by Liu *et al. via* a binary ethylenediamine/water solvent system during solvothermal treatment at 180 °C.[94] The solvent system was proposed to regulate the velocity and direction of crystal growth through a solvent-coordination molecular-template mechanism. Nanoribbons were obtained due to preferential crystal growth along the [001] direction. Catalytic screening highlighted the improved photoactivity of the resulting nanoribbons over Zn_2GeO_4 produced *via* solid state reaction (SSR) in producing CH_4 under UV illumination (300 W Xe arc lamp) in a CO_2/H_2O saturated glass reactor system. The better photocatalytic performance was attributed to (i) the higher surface area of the nanoribbons (28 m^2 g^{-1} *versus* 1 m^2 g^{-1} for the SSR material) (ii) the high quality single crystalline nature of the nanoribbons, which reduced electron–hole pair recombination, and (iii) the improved electron transport properties of the nanoribbons owing to their ultra-longitudinal dimension, and (iv) the geometry of the nanoribbons that permits rapid charge carrier diffusion to the oxide surface for CO_2 reduction. Photoactivity of these Zn_2GeO_4 nanoribbons could be further promoted by co-catalysts such as Pt, RuO_2 or a combination thereof, and even coupling to metal–organic frameworks such as ZIF-8 to enhance their CO_2 adsorption capacity.[95]

A similar synthesis was employed to prepare highly crystalline $In_2Ge_2O_7$(En) hybrid sub-nanowires, as shown in Fig. 4b, with diameters around 2–3 nm.[96] Although the nanowires outperformed a SSR prepared sample in CO_2 photoreduction by water vapour under UV illumination (300 W Xe arc lamp) within a gas-tight Pyrex glass reactor, CO was the only photoreduction product. A low temperature solution phase route, which does not require any surfactant, was reported for the preparation of single crystalline, hexagonal Zn_2GeO_4 nanorods for CO_2 photoreduction.[97] A mixed solution of Na_2GeO_3 and $Zn(CH_3COO)_2$ was heated at 40–100 °C to yield Zn_2GeO_4 nanorods with a regular, hexagonal prism geometry. As shown in Fig. 4c and d, nanorod dimensions were strongly dependent on synthesis temperature: nanorods around 400 nm long and 50 nm wide were obtained at 40 °C, while nanorods 250 nm long and 150 nm wide formed at 100 °C. Surprisingly, the prepared nanorods contained some blind holes due to the different crystal growth rate along the *c*-axis, as well as nanosteps in the surface of nanorods prepared at 100 °C. The absorption band edge of nanorods was blue-shifted (4.68 eV and 4.65 eV for 40 °C and 100 °C syntheses respectively) relative to that of SSR-prepared material (4.5 eV) due to quantum size effects, restricting their use to hard UV applications. Under illumination, Zn_2GeO_4
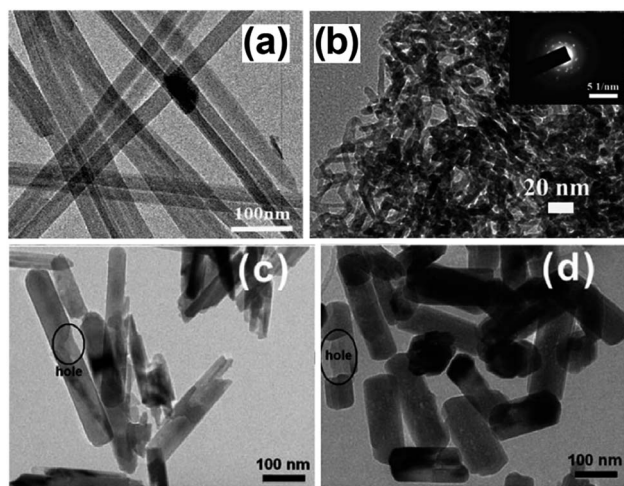
14492 | *J. Mater. Chem. A*, 2015, **3**, 14487–14516

This journal is © The Royal Society of Chemistry 2015

Fig. 4 TEM images of (a) Zn_2GeO_4 nanoribbons[94] and (b) $In_2Ge_2O_7$ sub-nanowires (inset: corresponding SAED pattern)[96] prepared by solvothermal treatment using a binary ethylenediamine/water solvent system, and Zn_2GeO_4 sub-nanowires prepared through solution phase route (c) at 40 °C and (d) 100 °C. Reproduced from ref. 97 with permission from The Royal Society of Chemistry.

nanorods outperformed those prepared by SSR towards photocatalytic H_2 generation and CO_2 reduction, with nanorods grown at 100 °C proving the most active for H_2 evolution owing to their greater crystallinity and the presence of surface nanosteps promoting charge separation. Conversely, the 40 °C synthesised nanorods exhibited better CO_2 photoreduction activity than their higher temperature analogues due to their higher surface area and CO_2 adsorption capacity.

Highly ordered one-dimensional TiO_2 NTs arrays have also been developed for photocatalytic applications.[98–101] These nanotube arrays have increasingly gained popularity as they: (i) exhibit a relatively high interfacial surface area (because of their internal and external surfaces); (ii) promote efficient transport of electrons owing to the thin walls of NTs; (iii) efficiently retard electron–hole recombination (which can occur up to ten times slower than equivalent nanoparticle films); and (iv) demonstrate improved photon absorption efficiency attributed to strong light scattering within the nanotube arrays.[98–103] The development of TiO_2 NTs arrays, including their synthesis and application, has been thoroughly reviewed by Rani *et al.*[103] spanning first generation (0.5 μm in length) to current 4th generation (~1000 μm) technologies. Electrochemical anodisation is the preferred method for nanotube arrays synthesis since it enables the nanotube dimensions to be precisely tuned through varying synthetic parameters such as electrolyte composition and anodising time. Varghese *et al.* prepared N-doped TiO_2 NTs arrays with pore size and wall thickness of 95 ± 13 nm and 20 ± 5 nm, respectively by anodising Ti foil in an NH_4F/water/ethylene glycol electrolyte at 55 V.[40] The resulting TiO_2 NTs arrays were then calcined and sputter coated with large, irregular patches of Pt, Cu or both metals, as co-catalysts, albeit little information was provided on the morphology and dispersion of these promoters, with the final material

containing between 0.4–0.75 at% N. Irradiation under natural sunlight and water vapour within a batch reactor, afforded CO_2 photoreduction to mainly H_2, CH_4 and other alkanes (*i.e.* C_2H_6, C_3H_8, C_4H_{10}, C_5H_{12} and C_6H_{14}), with olefins and branched paraffins also formed as minor products. Higher NTs calcination temperatures improved the photocatalytic activity, attributed to their higher crystallinity. Platinum promoted arrays generated more H_2 (almost 200 ppm cm^{-2} h^{-1}) than hydrocarbons, giving a total productivity of 273 ppm cm^{-2} h^{-1}, whereas the copper promoted array exhibited superior hydrocarbon production (~104 ppm cm^{-2} h^{-1}). Furthermore, the Cu–TiO_2 NTs arrays evolved five times more CO than Pt–TiO_2 arrays. Doubly promoted NTs arrays (Fig. 5) afforded a total hydrocarbon productivity of 111 ppm cm^{-2} h^{-1} without any detectable CO. It was concluded that Pt was more active for water reduction, while Cu was more efficient at reducing CO_2, their combination resulting in a strong synergy and maximal CO_2 conversion to hydrocarbons, with one of the highest visible light quantum efficiencies of 0.74%.

The synthesis of two-dimensional WO_3 nanosheets using a solid–liquid, phase arc discharge method for CO_2 photoreduction was recently reported by Chen *et al.*[104] Crystal growth was proposed to occur *via* the formation of a large number of 4–5 nm WO_3 seeds. These nanocrystals fused together into two-dimensional nanosheets during aging, while maintained a thickness <5 nm, with preferential growth in the [100] and [010] directions. The resulting band gap of these nanosheets (2.79 eV) was larger than that of commercial WO_3 powder (2.63 eV) due to quantum size effects, with their CB potential estimated to be more negative than the reduction potential for CO_2/CH_4 conversion. Conversely, the CB position of commercial WO_3 appeared more positive than the CO_2/CH_4 redox potential, which should hence disfavour CO_2 reduction. Indeed, visible light illumination (300 W Xe arc lamp equipped with a 420 nm cut-off filter) of the as-prepared nanosheets showed that they outperformed the commercial WO_3 powder in photoreducing
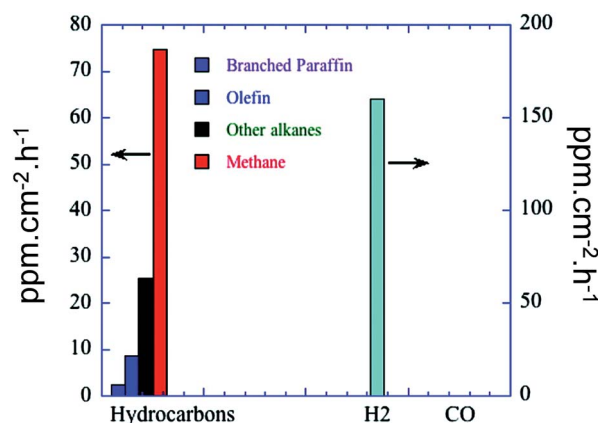

Fig. 5 Product formation of N-doped TiO_2 NTs arrays, calcined and sputtered coated with Pt and Cu. CO_2 photoreduction was conducted in a batch reactor under natural sunlight illumination in the presence of water vapour at 44 °C. Reprinted with permission from ref. 40. Copyright 2009 American Chemical Society.

CO_2 to CH_4 in a gas-tight system. Superior nanosheet photo-activity was therefore attributed to both their ultrathin geometry, expected to promote efficient charge carrier diffusion, and their more negative conduction potential. CO_2 adsorption can be enhanced through the use of alkali or alkaline earth basic oxides. Strontium promoted niobates prepared by conventional SSR have shown promise in CO_2 photoreduction by water vapour, but possess extremely low surface areas and are hence unsuitable for achieving high photoactivity. An alternative hydrothermal approach affords two-dimensional $SrNb_2O_6$ nanoplates around 12 nm thick and 5–300 nm across,[105] conferring a 20-fold increase in CO_2 adsorption capacity and quantum efficiency of 0.065% over 10 h, an order of magnitude higher than P25. In contrast to many studies, high selectivity to CO_2 reduction to CO and CH_4 *versus* competing H_2O reduction to H_2 was observed, alongside significant oxygen evolution. Transient photocurrent response measurements suggest that separation of photogenerated electron–hole pairs was rate-determining, with the nanoplate morphology facilitating charge-carrier diffusion to the surface and subsequent reaction with adsorbed CO_2 and water.

2.2.2. Porous structured photocatalysts. Mesoporous and hierarchical heterogeneous catalysts have proved superior to their non-porous analogues in a number of important chemical transformations, including catalytic cracking, selective oxidation, biomass valorisation and pollution abatement systems. Hence, it may be anticipated that porous semiconductor photocatalysts will likewise outperform their bulk counterparts. Such enhanced reactivity may reflect a combination of factors including the generally higher surface area of porous nanostructures, which in turn increases the number of active sites and thus photoconversion efficiency,[79,106–109] and high aspect ratios which assists rapid transport of photoexcited carriers to the catalyst surface, thereby suppressing competing bulk recombination processes.[107,109–111] Macropore incorporation into mesoporous architectures can confer additional benefits *via* increased light scattering and faster in-pore mass transport of sterically hindered reagents, finding particular application in the photodegradation of organic dyes.

Crystalline, porous structured Ga_2O_3 has been successfully synthesised by Park *et al.* employing a tetradecyl trimethyl ammonium bromide template.[107] Field emission scanning electron microscopy (FE-SEM) and transmission electron microscopy (TEM) images (Fig. 6), revealed the co-existence of macropores and mesopores througout the resulting mono-dispersed material. Subsequent photocatalytic screening showed that CO_2 conversion over this hierarchically porous Ga_2O_3 was much higher than that of reference Ga_2O_3 nanoparticles. Further investigations into CO_2 adsorption established that the porous Ga_2O_3 possessed a vastly superior CO_2 adsorption capacity, 300% higher than that of the bulk reference, accounting for its improved photoreduction of CO_2 to CH_4. Surfactant templating was also utilised to prepare mesoporous, micrometric ZnO spheres with the Pluronic P123 templating agent through hydrothermal treatment.[112] Individual ZnO spheres were composed of stacks of thin ZnO flakes, which created interparticle mesoporous voids. This mesoporous

architecture gave higher CO_2 conversion than the equivalent non-porous ZnO, and following Cu impregnation the mesoporous ZnO favored the selective production of CH_4 and CH_3OH. The utility of porous structures for CO_2 photoreduction to CH_4 has also been reported for titania,[79] albeit the surface area of the mesoporous TiO_2 decreased significantly upon subsequent nitridation to generate visible light active, N-doped TiO_2.

In recent years, a new synthetic protocol has been developed to create multicomponent, mesoporous photocatalysts for CO_2 reduction. Here an inorganic precursor is used to construct more thermally robust mesostructures.[113] The synthetic route of Yan *et al.* to prepare mesoporous $ZnGa_2O_4$ is illustrated in Fig. 7A. A powdered $NaGaO_2$ starting material was synthesised through a solid-state route, which formed colloidal particles upon dispersion in water. Weak surface repulsion between the resulting nanoparticles enabled their subsequent flocculation to form a mesoporous framework, followed by Na^+ and Zn^{2+} ion-exchange to yield a mesoporous $ZnGa_2O_4$ (visualised in Fig. 7B). The final material remained crystalline after the ion-exchange, obviating the need for hydrothermal treatment or high temperature calcination. The final $ZnGa_2O_4$ exhibited a mean pore diameter of 3.5 nm and surface area around 110 m^2 g^{-1}. Catalytic screening demonstrated that the mesoporous $ZnGa_2O_4$ was superior to $ZnGa_2O_4$ prepared through solid-state synthesis, with photogenerated CH_4 prevalent when a RuO_2 co-catalyst was employed. In common with many such studies there was no justification fo the choice of co-catalyst, nor its mode of operation, which was simply presumed to improve separation of photogenerated electron–hole pairs. This synthetic procedure was further adapted to prepare a $ZnAl_2O_4$-modified, mesoporous ZnGaNO visible light photocatalyst[111] from a $NaGa_{1-x}Al_xO_2$ precursor to form an amorphous mesoporous colloid template by flocculation. Following ion-exchange with Zn^{2+}, the resultant $Zn(Ga_{1-x}Al_x)_2O_4$ was hydrothermally treated to improve its crystallinity prior to nitridation; Al was claimed to enhance the thermal stability of the mesostructure. CO_2 photoreduction was negligible over the parent ZnGaNO (with or without $ZnAl_2O_4$ modification) without Pt doping to promote electron–hole separation. The superior performance of the $ZnAl_2O_4$ modified material was attributed to improved mass transport, increased basicity and hence CO_2 chemisorption, and narrowing of the band gap. Micro/mesoporous Zn_2GeO_4 and mesoporous zinc germanium oxynitride synthesised *via* the
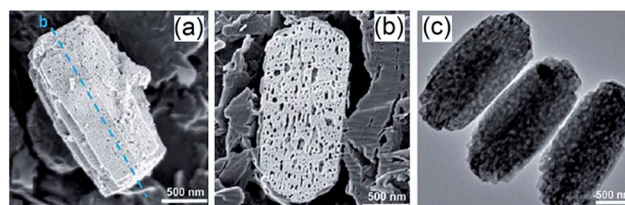

Fig. 6 FE-SEM images of (a) porous Ga_2O_3, (b) vertical cross-section of porous Ga_2O_3 fractured by ion beam and (c) TEM image of the porous Ga_2O_3. Reproduced from ref. 107 with permission from The Royal Society of Chemistry.

14494 | *J. Mater. Chem. A*, 2015, **3**, 14487–14516

This journal is © The Royal Society of Chemistry 2015

same method also evidenced superior CO_2 photoconversion compared to their solid state synthesised counterparts.[106,114]

Regular mesopore voids can also be created through the self-assembly of nanoparticles wherein the mesopores are formed at the junction between nanoparticles. This approach was successfully employed by Wang *et al.* to prepare sub-micron TiO_2–SiO_2 mesoporous composites.[108] These materials were obtained by atomising TiO_2 and SiO_2 nanocolloidal solutions of 20–45 nm particles into micron-sized droplets at elevated temperature. Solvent evaporation drove colloidal self-assembly to yield the mesoporous TiO_2–SiO_2 composite imaged by FE-SEM image in Fig. 8a. Cu doped variants were also produced by introducing $Cu(NO_3)_2$ into the colloidal precursor solution. Higher synthesis temperatures promoted TiO_2 nanocrystal segregation at the composite surface (Fig. 8b). The porous SiO_2 matrix ensured that TiO_2 dispersed across the composite surfaces as ∼20 nm crystals, rather than larger agglomerates. TiO_2–SiO_2 composites exhibited superior photoactivity to pure TiO_2 for CO_2 photoreduction to CO. Activity increased with processing temperature up to 1000 °C due to an increasing density of TiO_2 nanocrystals decorating the mesoporous framework, with a composite comprising 2 mol% TiO_2 and 0.01 mol% Cu giving the highest rate of CO_2 photoreduction. Mesoporous $In(OH)_3$ has also been prepared through a template-free hydrothermal treatment[110] resulting in the self-assembly of crystalline $In(OH)_3$ nanocubes. The introduction of mesoporosity enhanced CO_2 photoreduction to CH_4 by 20-fold relative to conventional $In(OH)_3$ crystallites attributed to the higher surface area and CO_2 adsorption affinity of the mesoporous variant.

Graphitic carbon nitride (C_3N_4), a metal-free polymeric semiconductor, has gained increasing popularity in photocatalysis for visible light application.[113,115–118] Switching the precursor from melamine to melamine chloride followed by rapid heating afforded porous C_3N_4:[119] Fig. 9 compares the platelet-like structure of melamine-derived C_3N_4 (g-C_3N_4) with the porous platelets obtained from the melamine chloride analogue, (p-g-C_3N_4) whose surface area was significantly higher (69 m^2 g^{-1} *versus* 1.7 m^2 g^{-1} for g-C_3N_4). Despite these textural differences the non-porous g-C_3N_4 outperformed the porous p-g-C_3N_4 during CO_2 the photoreduction to CO under visible light. This surprising result was attributed to the slightly broadened band gap and poorer crystallinity of p-g-C_3N_4, which may arise from a higher density of defects acting as electron–hole recombination centres. Porous C_3N_4 was also prepared by Mao *et al.* (denoted u-g-C_3N_4) from a urea precursor, which displayed superior CO_2 photoreduction activity relative to melamine-derived C_3N_4 (m-g-C_3N_4).[120] Akin to the findings of Dong and co-workers, porous u-g-C_3N_4 was less crystalline than the melamine analogue, with an order of magnitude higher surface area and slightly wider band gap. However, in this instance u-g-C_3N_4 exhibited superior photoactivity, presumably due to enhanced reactant adsorption and more efficient charge carrier separation. Under visible light, and in the presence of 1 M NaOH, u-g-C_3N_4 photoreduced CO_2 to a mixture of CH_3OH and C_2H_5OH, while m-g-C_3N_4 favoured C_2H_5OH with only trace methanol. Selective photocatalytic CO_2 reduction is hence achievable through tuning of material crystallinity and microstructure.

Table 1 shows that most mesoporous semiconductors possess modest surface area, however there is scope for enhancing these through their immobilisation onto higher area supports such as mesoporous silicas.[121,122] Such high area templates, albeit inert, facilitate dispersion of photoactive phases, thereby increasing the surface active site density and hence photoconversion efficiency. Yang *et al.* reported that TiO_2 supported on SBA-15 exhibited superior photoactivity to P25 during CO_2 photoreduction to CH_3OH.[122] The crystallite size of the dispersed TiO_2 increased with loading but remained smaller than that of commercial P25, however it is unclear how much titania was incorporated with the SBA-15 pore network *versus* external surface, and hence performance may have been sub-optimal. Further studies revealed that higher CH_3OH yields were achievable by Cu doping these TiO_2/SBA-15 catalysts. Li

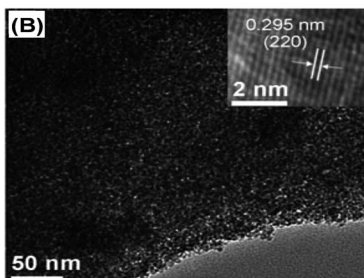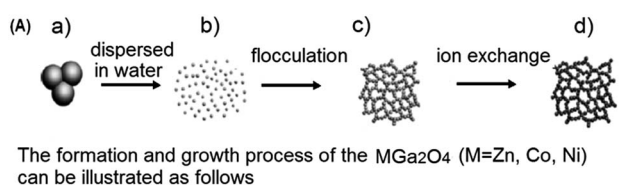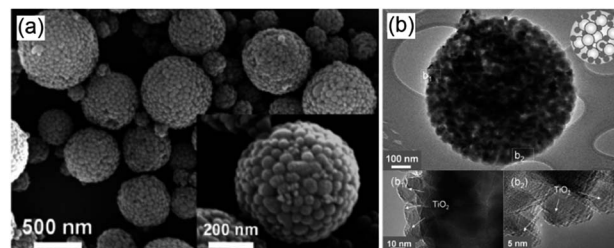**Fig. 7** (A) Schematic diagram showing the synthesis steps of preparing mesoporous $ZnGa_2O_4$ through mesoporous colloidal template and ion-exchange reaction and (B) TEM image of the resulting mesoporous $ZnGa_2O_4$ (inset: HR-TEM image of the crystal fringes). Reproduced with permission from ref. 113. Copyright 2010 Wiley.

Fig. 8 (a) FE-SEM and (b) TEM and HR-TEM images of mesoporous TiO_2–SiO_2 composites prepared at 800 °C. Reproduced from ref. 108 with permission from The Royal Society of Chemistry.
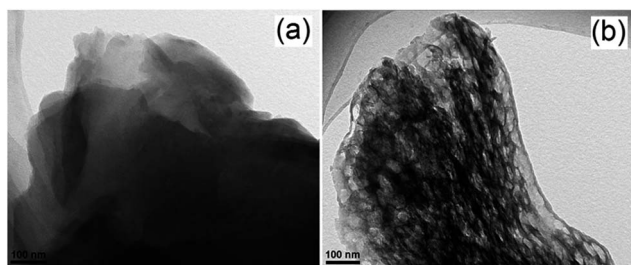
Fig. 9 TEM images of (a) non-porous g-C_3N_4, and (b) porous p-g-C_3N_4. Reproduced from ref. 119 with permission from The Royal Society of Chemistry.

et al. prepared TiO_2/mesoporous silica composites through a one-pot, sol–gel method.[113] The resulting material was more active than pure TiO_2 in photororeducing CO_2 to CO and CH_4, with Cu addition favouring CH_4 production.

2.2.3. Layered structured photocatalysts. Improvements in charge carrier separation and charge transfer for various photocatalytic applications have been sought for many years through the development of layered semiconductors, such as lamellar titanates and niobates.[124-127] Li *et al.* recently synthesised such layered materials for CO_2 photoreduction through the hydrothermal processing of KNb_3O_8 and HNb_3O_8.[128] In a typical synthesis, Nb_2O_5 powder in KOH solution was hydrothermally treated in the presence of a P123 Pluronic surfactant and the resulting precipitate was calcined to yield KNb_3O_8. Solid niobic acid, HNb_3O_8, was obtained through subsequent proton exchange of the KNb_3O_8 in nitric acid (KNb_3O_8 is isostructural with HNb_3O_8). As shown in Fig. 10a, HNb_3O_8 comprised two-dimensional $Nb_3O_8^-$ anion layers, constructed from edge-sharing NbO_6 octahedral units, with protons located in the interlayer spacing. Nanobelts of around 50 nm thickness were obtained during hydrothermal processing of KNb_3O_8, in contrast to the irregular micron size particles usually obtained from conventional SSR. Surface areas of the hydrothermal KNb_3O_8 and HNb_3O_8 materials of 29 m^2 g^{-1} and 39 m^2 g^{-1} respectively were higher than those prepared by SSR (2.7 m^2 g^{-1} and 6.5 m^2 g^{-1}) as a consequence of their layered

morphologies. CO_2 photoreduction by water vapour under UV illumination (350 Xe lamp) demonstrated enhanced performance of the layered niobates for CH_4 production within a sealed quartz tubular reactor, possibly due to more efficient charge carrier migration to the nanobelt surface compared with that of irregular particles. Methane productivity over HNb_3O_8 was twice that reported for KNb_3O_8, accredited to more effective water diffusion within the hydrophilic $HNbO_3O_8$ interlayers as illustrated in Fig. 10b, and hence a ready supply of protons to drive CO_2 reduction over the solid acid. Hydrothermal synthesis of $HNbO_3O_8$ thus afforded improved photoactivity due to both its thin nanobelt morphology and better water adsorption properties.

Expanded HNb_3O_8 interlayers were explored by Li *et al.* as a means to further boost photocatalysis through pillaring silica as a guest compound within the interlayer space.[129] A HNb_3O_8 precursor was first prepared by conventional SSR and subsequent proton exchange. HNb_3O interlayers were then expanded *via* n-dodecylamine, enabling access to tetraethyl orthosilicate. Calcination of the resulting material created a SiO_2-pillared HNb_3O_8 with XRD indicating that silica pillaring increased the interlayer spacing from 0.37 nm to 2.10 nm, facilitating their visualisation by TEM (Fig. 11). Pillaring also dramatically increased the niobic acid surface area from ∼7 to 197 m^2 g^{-1}, while simultaneously loweing the band gap from 3.5 eV to 3.3 eV. Under UV irradiation (350 W Xe lamp) under water vapour,
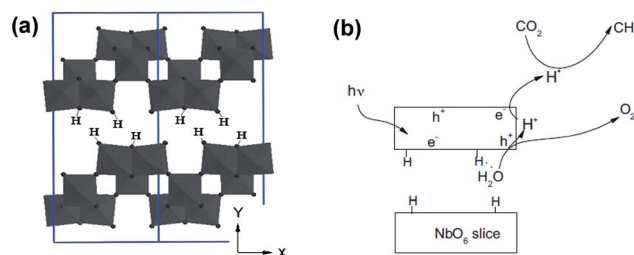

Fig. 10 Schematic depicting (a) the layered structure of HNb_3O_8, and (b) proposed mechanism of CO_2 photoreduction over HNb_3O_8. Reprinted from ref. 128, Copyright 2012, with permission from Elsevier.

Table 1 Textural properties of porous, structured photocatalysts and associated products of CO_2 photoreduction

Photocatalyst	Surface area/m^2 g^{-1}	Pore diameter/nm	Product
Ga_2O_3 (ref. 107)	43	3.8, 5–30	CH_4
1.5 wt% Cu/ZnO[112]	22	31.2	CH_3OH, CH_4, CO, H_2
0.12 wt% Pt/TiO_2 (ref. 123)	147	7.8	CH_4
0.84 at% N–TiO_2[123]	70	12.6	CH_4 (Pt)
$ZnGa_2O_4$ (ref. 113)	110	3.5	CH_4
$ZnAl_2O_4$/ZnGaNO[111]	53	15.2	CH_4
Zn_2GeO_4 (ref. 114)	91	1.2–2, 2–12	CH_4
ZnGeON[106]	36	—	CH_4
TiO_2–SiO_2 (ref. 108)	72	28.3	CO
$In(OH)_3$ (ref. 110)	65	9.5	CH_4
u-g-C_3N_4 (ref. 120)	40	—	CH_3OH, C_2H_5OH
45 wt%TiO_2–SiO_2 (ref. 122)	436	2–12	CH_3OH
0.5%Cu/TiO_2–SiO_2 (ref. 113)	386	—	CO, CH_4

and doping with 0.4 wt% Pt promoter, this SiO_2-pillared HNb_3O_8 proved superior to both the Nb_2O_5 precursor and non-pillared HNb_3O_8 layered structure for photoreducing CO_2 to CH_4 in a sealed quartz tubular reactor. Active sites of lamellar solid acids are considered to reside at the internal surfaces of interlayers.[130] Accordingly, Li and co-workers proposed that this enhanced photoactivity arose from increased active site accessibility within the HNb_3O_8 interlayers by CO_2 and H_2O. However, in common with many other studies, the simultaneous variation of physical and optical properties makes it hard to elucidate the principal origin of this enhancement. SiO_2-pillared HNb_3O_8 also outperformed the aforementioned HNb_3O_8 nanobelts. Additional investigations found that CH_4 production was lower over SiO_2-pillared KNb_3O_8 (prepared by cation exchange with K_2CO_3) than SiO_2-pillared HNb_3O_8, suggesting that water adsorption by the solid acid variant also played an important role in driving CH_4 formation.

Solid bases are well-established as CO_2 capture agents.[67,131–133] Accordingly, layered double hydroxides (LDHs) composed of $[M^{II}_{1-x}M^{III}_x(OH)_2]^{x+}$ cationic sheets with intercalated anions have been exploited for CO_2 photoreduction.[134,135] These materials are attractive because of their strong and tunable basicity, and hence good CO_2 adsorption capacity. The semiconducting nature, and hence photoabsorption properties, of LDHs can be tuned to some extent through careful selection of the intralayer M^{II} and M^{III} metal cations. Recent work from Sastre *et al.* showed that CO_2 photoreduction to CH_4 was enhanced by Zn/Ti or Zn/Ce LDHs,[135] presumably through increased CO_2 adsorption at the LDH surfaces facilitating subsequent photochemistry. Ahmed *et al.* prepared photoactive Zn^{2+}/Ga^{3+} LDH catalysts.[134] Under UV irradiation (500 W Xe arc lamp), the resulting $[Zn_3Ga(OH)_8]_2^+(CO_3)^{2-} \cdot mH_2O$ solid base was active for reducing CO_2 into CO and CH_3OH as primary and secondary products respectively, employing a closed, circulating system pressurised with a mixture of 2.3 kPa CO_2 and 21.7 kPa H_2, *i.e.* highly reducing conditions wherein commercial application would require an independent photocatalytic or electrochemical hydrolysis process to supply hydrogen, or close proximity to a fossil fuel derived syn gas feed. Copper incorporation into the LDH to form a $[Zn_{1.5}Cu_{1.5}Ga(OH)_8]_2^+$ $(CO_3)^{2-} \cdot mH_2O$ material improved selectivity towards CH_3OH threefold, rendering it the major product. Control experiments

in the absence of CO_2 suggested that at least some of the observed reactivity was associated with the conversion of CO_3^{2-} ions originating within the parent LDH, although this could not account for the total product yield. Replacing Ga^{3+} with Al^{3+} to create a $[Zn_3Al(OH)_8]_2^+(CO_3)^{2-} \cdot mH_2O$ LDH enhanced overall photoconversion efficiency, but favoured CO formation (even after Cu^{2+} incorporation). These layered catalysts were reported active for 20 h continuous CO_2 photoreduction, although methanol productivity declined over time. In an effort to boost selectivity towards methanol, the interlayer CO_3^{2-} anions were exchanged for $[Cu(OH)_4]^{2-}$ anions, thereby creating a $[Zn_{1.5}$-$Cu_{1.5}Ga(OH)_8]_2^+(CO_3)^{2-} \cdot mH_2O$ material[136] with a methanol yield almost three times that achievable over the carbonate counterparts. Copper was thus hypothesised as the active photocatalytic site, with the localisation of Cu sites within the interlayers facilitating their accessibility to CO_2, while the replacement of CO_3^{2-} with $[Cu(OH)_4]^{2-}$ counterions significantly decreased the band gap of the resulting LDH while expanding the interlayer spacing, both factors likely contributing towards the enhanced photoactivity of the copper anion doped variant.

2.2.4. Hierarchical ordered photocatalysts. Three-dimensional, hierarchical photocatalysts with novel properties arising from their unique morphology have also been exploited to further optimise photocatalytic performance. Many studies have shown that such complex architectures, typically possessing high surface areas and diverse pore-interconnectivities, offer enhanced catalytic activity relative to their bulk, nanoparticulate or monomodal nanoporous counterparts.[137] The unique surface and textural characteristics of these superstructures can also increase photon absorption, leading to enhanced quantum efficiency.[138–143] To date, semiconductors with diverse three-dimensional, hierarchical structures have been developed for harvesting solar energy, including ZnO nanowire forests,[143] Si/InGaN core–shell nanowire arrays,[142] TiO_2/ZnO/CuO forest-like architectures,[140] Bi_2O_3/Bi_2WO_6 microclews,[144] N-doped Bi_3NbO_7 peony-like architectures,[145] flower-like Ta_2O_5,[146] $Bi_{12}TiO_{20}$,[147] $Bi_{12}TiO_{20}$/TiO_2,[148] Nb_3O_7F,[149] Bi_2O_3,[150] and NiO–CdS architectures,[151] CdS@ZnO and CdS@Al_2O_3 urchin-like heteroarrays,[91] N-doped $(BiO)_2CO_3$ microspheres,[141] Fe_3O_4/WO_3 core–shell structures,[152] WO_3 hollow dendrites, spheres and dumbbells,[153] porous TiO_2 hollow microspheres,[138,154] and γ-TaON urchin-like hollow spheres.[139] Such complex structures are generally created through the self-assembly of nanoscale building blocks, such as nanosheets and nanorods, *via* hydrothermal routes.[91,141,144–152] In some instances, pore networks created within hierarchical networks not only increase the total surface area, but also serve to accelerate reactant/product diffusion to/from active centres.[141,154] While relatively few studies have targeted the development of hierarchical structures for CO_2 photoreduction, a number of promising three-dimensional nanostructures have been created for solar fuels production.

Highly ordered, sheaf-like, hyperbranched Zn_2GeO_4 superstructures were prepared in the presence of ethylenediamine through a solvothermal method by Liu *et al.*[155] The FE-SEM image in Fig. 12a highlights 3–4 μm sheaf-like features which
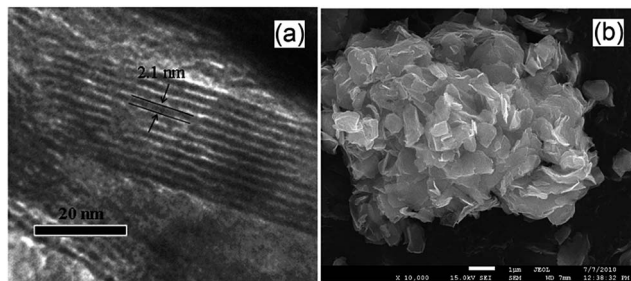

Fig. 11 (a) TEM and (b) SEM images of SiO_2-pillared HNb_3O_8. Reprinted with permission from ref. 129. Copyright 2009 American Chemical Society.

This journal is © The Royal Society of Chemistry 2015

J. Mater. Chem. A, 2015, **3**, 14487–14516 | **14497**

assembled from closely packed, well-aligned nanowires with fantails oriented toward the center and projecting radially outwards. This unique morphology was proposed to arise through a crystal-splitting growth mechanism, with the degree of splitting a function of reaction time, precursor concentration and solvent. In order to improve the visible light performance of the normally large band gap Zn_2GeO_4, these as-prepared fusiform bundles were subject to nitridation at 700 °C, resulting in a yellowish zinc germanium oxynitride ($Zn_{1.7}GeN_{1.8}O$) photocatalyst. While the bundle morphology of the parent $Zn_{1.7}GeN_{1.8}O$ precursor was retained after this high temperature treatment, an added benefit was a concomitant significant increase in surface roughness (Fig. 12b), which doubled the $Zn_{1.7}GeN_{1.8}O$ surface area relative to the Zn_2GeO_4 parent. Under visible light illumination (300 W Xe arc lamp equipped with a 420 nm cut-off filter), and only upon promotion with Pt or RuO_2 co-catalysts, this hierarchically structured $Zn_{1.7}GeN_{1.8}O$ material showed good ambient pressure CO_2 photoreduction to CH_4, albeit with an apparent quantum efficiency still only approaching 0.024%. It is noteworthy that the CH_4 yield reached saturated around 6 h, possibly due to reversible adsorption of reactive intermediates.

Hexagonal nanoplate-textured micro-octahedral Zn_2SnO_4 were synthesised through a hydrothermal treatment in the presence of L-tryptophan.[156] The resulting material comprised ordered and uniform micro-octahedra with edges of approximately 3 μm (Fig. 13a). At higher magnification, it is apparent that each micro-octahedron is densely packed with ~50 nm thin, hexagonal nanoplates Fig. 13b. These nanoplates are vertically arranged within octahedra such that they lie parallel to neighbouring edges. The octahedral geometry was proposed a consequence of L-tryptophan impeding reaction along the [111] direction, favouring faster nucleation and growth in the [100] direction. The resulting hierarchical nanoplate/micro-octahedron morphology blue-shifted the Zn_2SnO_4 band gap from the bulk value of 3.67 eV to 3.87 eV, yet delivered exclusively CH_4 production at 20 ppm g^{-1} from CO_2 under UV irradiation within a gas-tight Pyrex glass cell, albeit for only 1 h in the absence of promoters. This far exceeded the photoactivity of bulk Zn_2SnO_4 (1.5 ppm g^{-1}), smooth Zn_2SnO_4 micro-octahedra (4.7 ppm g^{-1}) or Zn_2SnO_4 atactic particles (2.4 ppm g^{-1}) prepared without L-tryptophan. This rate enhancement was ascribed to such superstructures acting as light-scattering centres promoting photon harvesting, in combination with the nanoplate morphology promoting electron transport along
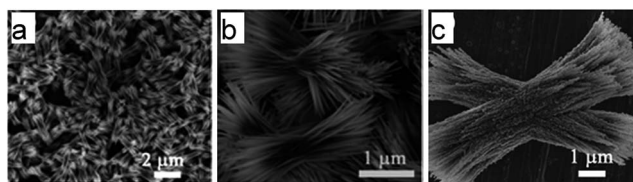
individual plates, and the open nanoplate-/micro-octahedron architecture which facilitated rapid molecular diffusion.

Hierarchical, hollow Bi_2WO_6 microspheres, which were constructed from crossed nanosheets prepared through an anion exchange method by Cheng et al., successfully photo-reduced CO_2 to CH_3OH under visible light irradiation.[157] As depicted in Fig. 14, the synthesis involved anion exchange of BiOBr solid microspheres, prepared from $Bi(NO_3)_3$ and a $[C_{12}Mim]Br$ ionic liquid, with Na_2WO_6 under hydrothermal conditions at 160 °C. BiOBr and Bi_2WO_6 comprise crystalline layered structures consisting of alternating $(Bi_2O_2)^{2+}$ slabs separated by intercalating anion layers. Since the solubility of Bi_2WO_6 was lower than that of BiOBr, thin layers of Bi_2WO_6 formed at the $BiOBr^-$ surfaces during the exchange process. Owing to the slower diffusion of WO_4^{2-} versus Br^-, a fast, continuous outflow of Br^- through the Bi_2WO_6 shell resulted in the formation of hollow cores over a prolonged period. These 2–5 μm diameter, hollow microspheres were themselves mesoporous, with a surface area far higher than that of Bi_2WO_6 prepared by a solid state route (Bi_2WO_6 SSR). Hollow Bi_2WO_6 microspheres generated around 25 times more CH_3OH from CO_2 photoreduction by water than Bi_2WO_6 SSR at under visible light (300 W Xe arc lamp equipped with a 420 nm cut-off filter). This performance was notably achieved without the aid of noble metal co-catalysts. As in the previous examples, this enhanced photocatalysis was attributed to the higher surface area and CO_2 adsorption affinity (eight times that of Bi_2WO_6 SSR) of the hierarchical structure.

An exciting biomimetic approach was recently adopted by Zhou et al. to prepare hierarchical, three-dimensional perovskite titanates, $ATiO_3$ (A = Sr, Ca, Pb), for CO_2 photoreduction.[158] In an effort to move one-step closer to artificial photosynthesis, fresh Cherry Blossom green leaves were employed as a structure-directing agent to prepare inorganic photocatalysts via a modified sol–gel protocol; natural leaves possess high porosity, connectivity and surface areas, tailored to facilitate efficient gas diffusion, water transport and the harnessing of solar energy. The success of this synthesis was evidenced by the FE-SEM images in Fig. 15a and b, wherein the resulting $SrTiO_3$ exhibited a macroporous venation network characteristic of the parent leaves. Higher magnification TEM imaging revealed the network walls consisted of a
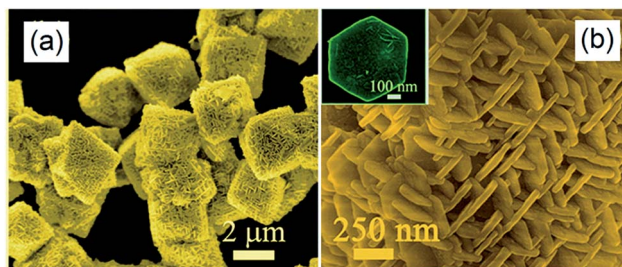

Fig. 12 FE-SEM images of (a and b) sheaf-like Zn_2GeO_4 superstructure solvothermally treated for 12 h, and (c) $Zn_{1.7}GeN_{1.8}O$ prepared through high temperature nitridation of Zn_2GeO_4 fusiform bundles. Reproduced from ref. 155 with permission from The Royal Society of Chemistry.

Fig. 13 FE-SEM images of the nanoplate/micro-octahedron Zn_2SnO_4 at (a) lower magnification and (b) at higher magnification. The inset of (b) shows an isolated hexagonal nanoplate. Reprinted with permission from ref. 156. Copyright 2012 American Chemical Society.
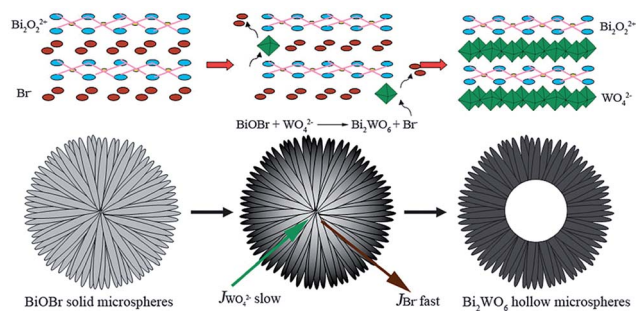
Fig. 14 Schematic of hollow Bi_2WO_6 microspheres formation through anion exchange of solid BiOBr microspheres. Reproduced from ref. 157 with permission from The Royal Society of Chemistry.

mesoporous array of crystallites (Fig. 15c and d). Such biomimetic $SrTiO_3$ and $CaTiO_3$ architectures outperformed corresponding reference titanates in CO_2 photoreduction to CO (major product) and CH_4 (secondary product) during UV illumination (300 W Xe arc lamp) under water vapour in a gas closed circulation system and 80 kPa of CO_2. Incorporation of Au, Ag and Cu into these hierarchical titanates enhanced their photoactivity, and also led to the evolution of trace C_2H_4 and C_2H_6, although the latter were proposed to arise *via* photocatalytic non-oxidative coupling of CH_4 rather than direct CO_2 photoreduction.[159]

The excellent performance of these leaf-architectured titanates presumably reflects their highly interconnected macroporous-mesoporous structure, which promotes gas diffusion in addition to increasing surface active sites. This sophisticated architecture may also enhance light absorption in a manner similar to that of natural leaves, by which incident light is scattered and transmitted into deeper layers of the network, thereby increasing the quantum efficiency and hence photocatalytic activity.

2.2.5. Hybrid structured photocatalysts. As touched upon in the preceding sections, semiconductor photocatalysts can be coupled with other materials which may comprise efficient charge carrier components (electron donor or acceptor), such as semiconductors, metal oxides or zeolites. Such combinations offer hybrid photocatalyst with superior physicochemical or optical properties to the parent active phase, *e.g.* a higher dispersion of active centres, enhanced accessibility of catalytic centres (*cf.* hierarchical architectures) or novel band structures. For instance, two semiconductors (SC) with different band gaps and valence/conduction band energy levels can be combined to create a staggered type II band structure as depicted in Fig. 16.[160] When light is absorbed by a small (visible) band gap semiconductor (SC_1), interparticle electron transfer can occur, in which photogenerated electrons are injected into the CB of a large band gap (SC_2) semiconductor, while photogenerated holes remain in the valence band (VB) of SC_1, thereby effecting charge separation through spatial localisation, and hence maximising the lifetime of photoinduced charge carriers and photocatalytic efficiency. Direct particle-to-particle contact is generally held to be crucial for efficient operation of such hybrid systems.[161]
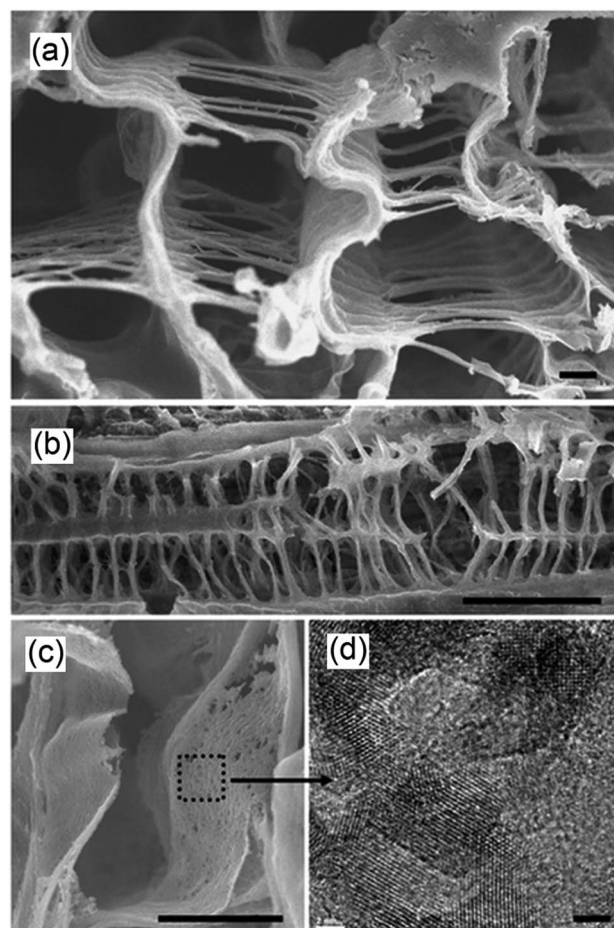

Fig. 15 FE-SEM images showing (a) the cross section of the porous venation architecture of $SrTiO_3$ (scale bar, 1 μm) (b) cross section of the porous network axially (scale bar, 10 μm), (c) magnified image of the wall of the network (scale bar, 1 μm) and (d) TEM image showing the mesoporous structure of $SrTiO_3$ (scale bar, 2 nm). Reprinted by permission from Macmillan Publishers Ltd ref. 158, copyright 2013.

2.2.5.1. Inorganic hybrid photocatalysts. A number of such SC_1/SC_2 hybrid systems have been developed for CO_2 photoreduction. Wang *et al.* prepared $CdSe/Pt/TiO_2$ heterostructures using commercially available CdSe quantum dots (QDs) of two different sizes (2.5 nm and 6 nm) and commercial P25 titania.[162] The resulting heterostructures, containing 0.5 at% Pt and 1 at%
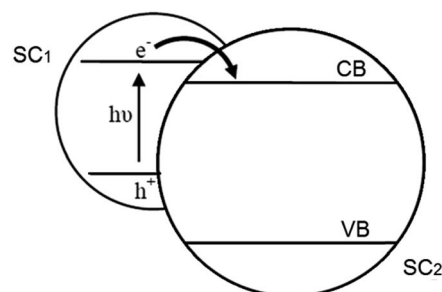

Fig. 16 Electron transfer pathway in a SC/SC hybrid system. Adapted from ref. 160, Copyright 1995, with permission from Elsevier.

Cd, were active for the photoreduction of CO_2 to CH_4 and CH_3OH (respective major and minor products) under visible light irradiation, with trace H_2 and CO also reported; neither Pt/TiO_2 or CdSe components were individually active under identical reaction conditions. Consequently, the observed visible light photoactivity of the semiconductor heterostructures must arise from a synergy between CdSe and TiO_2. It was proposed that photoexcited electrons promoted into the CB of CdSe under visible light irradiation, were subsequently injected into the CB of TiO_2, increasing their liftime and probability of transfer to CO_2. However, these composites deactivated after 4–6 h irradiation, most likely due to oxidation of the QDs by the accumulated photoinduced holes in the VB of CdSe.

In other work, coupling of AgBr with P25 was also undertaken to form nanocomposites active for reducing CO_2 under visible light,[163] wherein the indirect band gap of AgBr, which spans wavelengths between 450–700 nm, was held responsible for the visible light activity. This hybrid was synthesised utilising a cetyltrimethylammonium bromide (CTAB) surfactant stabiliser to create well-dispersed AgBr NPs (of around 5 nm) decorating the surface of P25. The nanocomposites exhibited excellent visible light photoactivity (150 W Xe lamp with a 420 nm cut-off filter) and photostability in the presence of aqueous $KHCO_3$, relative to pure AgBr, with CH_4 as the major product together with CH_3OH, CH_3CH_2OH and CO under high CO_2 pressure (7.5 MPa). A composite containing 23.2 wt% of AgBr exhibited optimum performance, with the photocatalytic mechanism again proposed to involve visible light excitation of electrons into the AgBr conduction band and subsequent transfer into the TiO_2 CB with attendant charge separation. In addition to increasing charge carrier lifetime, these hybrid structures also impeded the formation of metallic Ag through photolysis, as was observed for pure AgBr.

Qin *et al.* followed a similar route employing CTAB to produce 14 nm CuO/TiO_2 composite nanostructures,[164] although here UV irradiation in the presence of methanol (rather than water) resulted in CO_2 photoreduction to methyl formate within a slurry reactor. A 1 wt% CuO/TiO_2 composite calcined at 450 °C exhibited the highest photoactivity, outperforming both pure TiO_2 and composites synthesised in the absence of CTAB, suggesting a role for both charge separation and particle size effects. Liu *et al.* also explored the synergy between copper and titania heterojunctions, employing a sol–gel route to prepare Cu_2O/TiO_2 composites which demonstrated superior photoactivity over pure TiO_2 in photoreducing CO_2 to CH_4 in a stirred batch, annular quartz reactor under 1 bar of CO_2 and low power (32 W) UVA illumination.[165] XPS and pulse chemisorption measurements identified the presence of a two-dimensional Cu_2O species decorating the surface of titania at extremely low doping levels (0.03 wt% Cu). Higher copper loadings resulted in a structural transformation to three-dimensional Cu_2O crystallites, which reduced the efficiency of photoinduced electron transfer from TiO_2 to Cu_2O, and hence lowered their activity. TiO_2 has also been coupled with iron to form $FeTiO_3/TiO_2$ hybrids able to photoreduce CO_2 to CH_3OH under high power UV (500 W Xe lamp) and visible light irradiation under basic conditions.[166] Materials synthesised with 20 mol% Fe gave the highest rate of CO_2 reduction. Under UV illumination, photoinduced electrons were proposed to transfer from the (higher energy) CB of TiO_2 to that of $FeTiO_3$, with photoinduced holes returned from the VB of $FeTiO_3$ to that of TiO_2, charge separation again inferred as improving the overall photoactivity. In contrast, under visible light irradiation, electrons were photoexcited into the $FeTiO_3$ CB, resulting in a partially vacant $FeTiO_3$ VB, which was charge compensated for by the consequential movement of electrons from the almost isoenergetic TiO_2 VB, leaving residual holes in the TiO_2 VB, and net electron–hole charge separation across the two semiconductors. Efforts have been made to couple TiO_2 with CdS and Bi_2S_3 in order to photoreduce CO_2 to CH_3OH.[165] Li *et al.* precipitated CdS or Bi_2S_3 onto TiO_2 NTs to yield visible light active CdS/TiO_2 and Bi_2S_3/TiO_2 heterostructures, thereby delivering improved photoactivity relative to P25 or bare TiO_2 NTs (although activities were not normalised to take into account the two-fold higher surface areas of the nanorod morphologies). Photoinduced electrons from the CB of CdS or Bi_2S_3 could be injected into that of TiO_2 to achieve efficient charge separation. Nevertheless, these complex heterojunction nanorods failed to generate more CH_3OH than their respective pure CdS and Bi_2S_3 bulk analogues.

$CuO–Cu_2O$ thin film nanorod arrays prepared by Chadimkhani *et al.* were recently shown to photoreduce CO_2 into CH_3OH under simulated solar irradiation (AM 1.5) without a co-catalyst *via* photoelectrocatalysis.[167] Coupling of such small band gap semiconductors is advantageous in exploiting a larger fraction of the visible light region of the solar spectrum than achievable by either alone. CuO nanorods were first thermochemically grown over a Cu substrate, following which Cu_2O crystallites were electrodeposited on the nanorod surfaces to generate a CuO core/Cu_2O shell hybrid thin film which outperformed a compact Cu_2O electrodeposited film. This enhancement may reflect more efficient transfer of photoinduced electrons from the CB of the Cu_2O shell to that of the CuO core and consequent increased probability of photoinduced electrons reacting with CO_2. Such a model necessitates that the tips of CuO nanorods are exposed to a CO_2 saturated aqueous environment. The $CuO–Cu_2O$ thin film was reported to generate CH_3OH at a potential of only −0.2 V *vs.* SHE, lower than the standard redox potential for CO_2/CH_3OH (−0.38 V *vs.* SHE), a feature characteristic of p-type semiconductors (such as CuO and Cu_2O).

Copper oxide has also been employed by In *et al.* to form hollow $CuO–TiO_{2−x}N_x$ hybrid nanocubes that are effective for photoreducing CO_2 to CH_4.[168] As shown in Fig. 17a, Cu_3N nanocubes, synthesised through the thermal decomposition of $Cu(NO_3)_2$ in octadecylamine at 240 °C, were employed as the templating agent for subsequent TiO_2 deposition on their external surfaces through slow hydrolysis of titanium *n*-butoxide. The initial Cu_3N nanocubes were uniform in shape and around 27 nm across (Fig. 17b), and underwent significant roughening following TiO_2 coating (TiO_2@Cu_3N) as apparent in Fig. 17c. Subsequent heat treatment of the TiO_2@Cu_3N powder at 450 °C under air transformed these phase-separated structures into hollow $CuO–TiO_{2−x}N_x$ hybrid nanocubes (Fig. 17d–f).

The final material was composed of hollow, truncated cuboidal CuO hollow cubes of ∼57 nm diameter, decorated by small $TiO_{2-x}N_x$ particles. FE-SEM imaging confirmed the cubic morphology and hollow core of this hybrid material (Fig. 17g–f). The authors proposed that TiO_2 crystallised onto the surfaces of Cu_3N during thermal processing, but did not fully encapsulate the underlying nanocubes, permitting O_2 to diffuse into, and oxidise, the Cu_3N surface. Assuming that the inward rate of atomic oxygen diffusion is slower than the outward diffusion of N_2, high temperature treatment would drive the formation of hollow cores through the Kirkendall effect.[169] As nitrogen atoms diffuse outward, they are able to react with TiO_2 and hence form an oxynitride $TiO_{2-x}N_x$ phase. Under simulated solar illumination and water vapour, this particular hybrid composite photoreduced CO_2 to CH_4, and C_2H_6, C_3H_8 and C_4H_{10} as minor products. The hollow $CuO–TiO_{2-x}N_x$ hybrid nanocubes outperformed P25, CuO (annealed Cu_3N), $CuO@TiO_2$, Cu_3N and $TiO_2@Cu_3N$ in the photocatalytic generation of CH_3OH, likely due to their improved visible light absorption characteristics and the synergy between CuO and $TiO_{2-x}N_x$.

2.2.5.2. Organic hybrid photocatalysts. A hybrid catalyst composed of a Nafion (perfluorinated polymer with sulfonate groups, Nf) overlayer on TiO_2 with Pd co-catalyst was prepared by Kim *et al.* for CO_2 photoreduction[170] as illustrated in Fig. 18a. Pd was first impregnated onto P25, and subsequently coated with Nafion. The rationale for integrating Nafion with a photoactive semiconductor was that the superacidic polymer, which exhibits excellent proton conducting behaviour, would facilitate proton-coupled multielectron transfer (PCET) pathways during product (hydrocarbon) formation, thereby improving net CO_2 reduction. It was also believed that Nafion might inhibit the reoxidation of photoreduction products, and as a fluorinated polymer, be stable towards photocorrosion and redox reactions and thus a good host support. After catalyst pre-cleaning and UV irradiation the hybrid Nf/Pd–TiO_2 facilitated CO_2 photoreduction to CH_4, C_2H_6 and H_2 (and trace C_3H_8) in a sodium carbonate aqueous solution. As shown in Fig. 18b, CO_2 reduction was highly sensitive to reaction pH, with photoactivity increasing at lower pH, the higher H^+ concentration aiding product generation. In the presence of Nafion, considerably more CH_4 was generated at pH 3 and 11 but the effect was less prominent at pH 1. However, Nafion significantly enhanced ethane production at pH 3 and 1, with propane only observed over the Nf/Pd–TiO_2 hybrid photocatalyst. The observation that Nafion favours longer chain hydrocarbons suggest that it may stabilise CO_2 reduction intermediates in a manner that promotes sequential multi-electron transfer. Additional experiments with Nf/Pd–TiO_2 under natural sunlight only resulted in CH_4, C_2H_6 and C_3H_8 formation.

Sensitising large band gap semiconductors with transition metal complexes is another approach to designing visible light active materials.[171–173] Yuan *et al.* recently demonstrated the utility of a $Cu[(bpy)_2]^+$ dye-sensitised TiO_2 hybrid system for CO_2 photoreduction.[174] To obtain an air stable Cu complex, the 6- and 6′-position of the 2,2′-bipyridine (bpy) ligand were modified with a methyl group to protect the surroundings of the labile Cu(I) centre. This ligand was also designed to terminate in
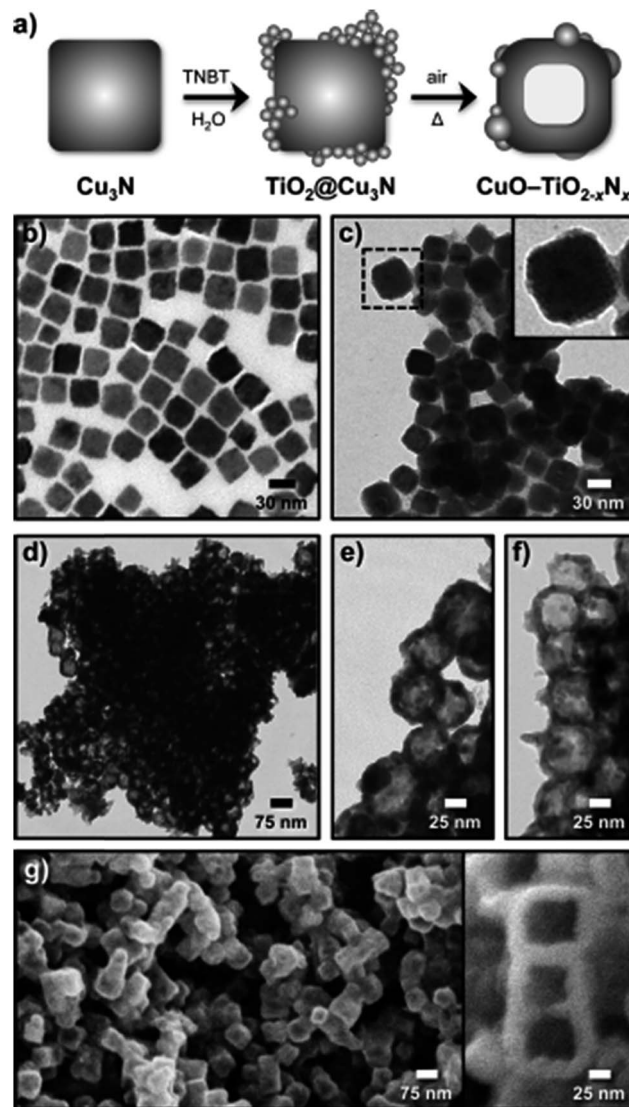

Fig. 17 (a) Schematic for the synthesis of hollow $CuO–TiO_{2-x}N_x$ hybrid nanocubes, and associated TEM images of (b) Cu_3N nanocubes, (c) $TiO_2@Cu_3N$ nanocubes, (d)–(f) hollow $CuO–TiO_{2-x}N_x$ hybrid nanocubes at different magnifications, and (g)–(h) FESEM images of the hollow hybrid nanocubes. Reproduced with permission from ref. 168. Copyright 2012 Wiley.

cyanoacetic acid moieties, thus enabling efficient anchoring of the metal complex onto the semiconductor surface. The Cu(I) complex modified P25 hybrid successfully photoreduced CO_2 with water vapour into CH_4 in a gas–solid reaction system under visible light illumination. It is likely that the Cu(I) complex was responsible for harnessing photons from visible light, with the resulting photoexcited electrons rapidly injected into the conduction band of the visible-inactive TiO_2, thereby prolonging the lifetime of photoinduced electrons to drive CO_2 reduction.

A visible light hybrid photocatalyst system, which utilised a naturally occurring enzyme CO dehydrogenase (CODH 1) to reduce CO_2, was developed by Woolerton *et al.*[175,176] This enzyme was homodimeric, such that each sub-unit contained a buried
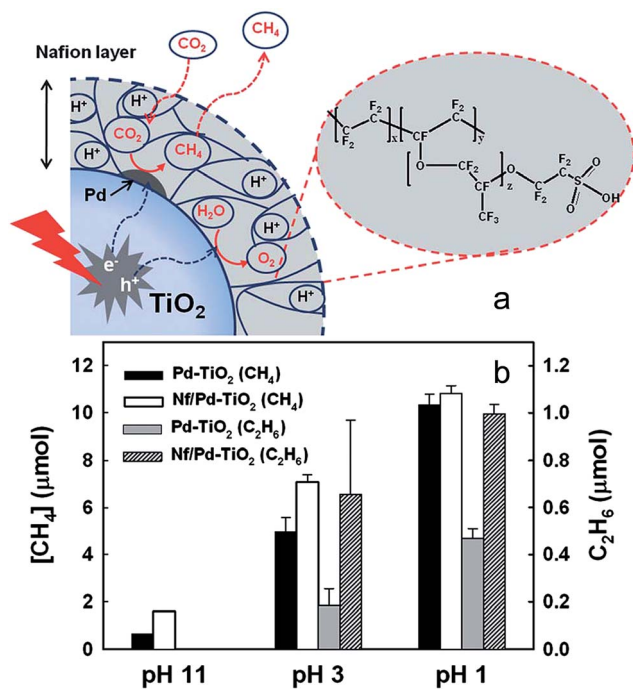
Fig. 18 (a) Schematic of CO_2 photoreduction on Nf/Pd–TiO_2 nanoparticles and (b) CH_4 (at 5 h) and C_2H_6 (at 1 h) production at different pH ranges on Pd–TiO_2 and Nf/Pd–TiO_2 NPs under UV illumination ($\lambda >$ 300 nm) in the presence of 0.2 M Na_2CO_3 aqueous solution. Catalyst concentration was fixed at 1.5 g L^{-1} (with 1.0 wt% Pd and 0.83 wt% Nafion). Reproduced from ref. 170 with permission from The Royal Society of Chemistry.

[Ni4Fe–4S] active site, wired to the protein surface through a series of [4Fe–4S] clusters that were also responsible for relaying electrons in and out of CODH 1. Fig. 19 illustrates the complete photosystem comprising CODH 1 modified, and Ru dye (RuP) sensitised, P25 NPs. During visible light irradiation, photoexcited electrons generated through metal-to-ligand charge-transfer on the RuP dye could be injected into the CB of TiO_2 and transferred through the [4Fe–4S] clusters to the CODH 1 active sites, with the resulting photo-oxidised RuP regenerated *via* 2-(*N*-morpholino) ethanesulfonic acid (MES) as a sacrificial electron donor. It was proposed that the reduction process was initiated through CO_2 binding as a bridging ligand between the Ni and dangling Fe atom of the enzyme. Under visible light illumination, TiO_2 thus functioned as a medium for relaying electrons between the dye and enzyme. It is noteworthy that CODH 1 usually oxidises CO to CO_2, but that the enzyme can be driven to catalyse the reverse reaction by applying a small overpotential.[177] Further investigations revealed P25 as the preferred semiconductor with respect to ZnO, $SrTiO_3$, rutile and anatase TiO_2.[175] Photoactivity was further enhanced through the addition of another sacrificial electron donor, ethylenediaminetetraacetic acid (EDTA). To improve CODH 1 attachment to titania, P25 was modified with various molecules, including polymyxin B sulphate and glutamic acid, albeit to no effect. On the other hand, functionalisation with *o*-phosphorylethanol led to a significant decrease in activity. Although this

particular system was capable of photoreducing CO_2 to CO, the photoconversion efficiency was lower than expected, and it was sensitive to O_2 passivation.[175,176] Photoactivity decreased after 4 h on-stream, potentially due to the difficulty in regenerating oxidised RuP, or the ineffectiveness of CODH 1 in harnessing electrons for activating CO_2.

2.2.5.3. Carbonaceous media hybrid photocatalysts. Carbon nanomaterials, such as activated carbons, carbon monoliths, carbon NTs, graphene and graphites[178,179] are promising candidates for catalyst supports, offering low cost, robust mechanical strength, high surface area, excellent porosity, chemical inertness and high electron conductivity. Moreover, carbons are amenable to the efficient recovery of precious metal promoters *via* combustion, and their surfaces may be readily functionalised by physical or chemical treatments, thereby modifying the resulting performance of hybrid catalysts. Significant work has been undertaken to integrate photoactive materials with carbonaceous media such as carbon NPs and graphene to deliver improve photocatalysts.

Covalently-functionalised carbon quantum dots (QDs) absorb and emit strongly in the visible light region.[180–183] Because of these unique electronic properties, surface-passivated carbon QDs are a promising visible light harvesting medium. Surface-functionalised carbon NPs prepared by Cao *et al.* were active in photoreducing CO_2 under visible light illumination.[184] Sub-10 nm carbon NPs were functionalised with oligomeric poly(ethylene glycol) diamine (PEG_{1500N}), rendering the resulting nanoparticles photoactive and water soluble. PEG-functionalised carbon QDs readily generated surface confined electrons and holes under irradiation that recombined radiatively (Fig. 20). This recombination process can be quenched by either electron donors or acceptors. Efficient charge separation and supressed radiative recombination was achieved through coated these surface-functionalised carbon NPs with Au or Pt through solution-phase photolysis; subsequent exposure to a light source would channel photogenerated electrons into the resulting metal nanoparticles, thereby prolonging the lifetime of charge carriers required for subsequent CO_2 reduction. Under visible light irradiation (425–720 nm), and in the presence of water, metal decorated and surface-functionalised carbon NPs proved active for photoreducing CO_2 to formic acid, although product analysis relied upon solution phase ^1H and ^{13}C NMR spectroscopy, and hence was unable to quantify the
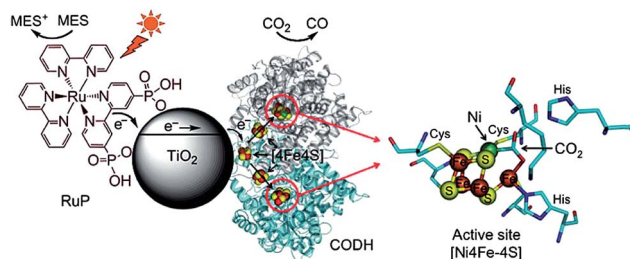

Fig. 19 Schematic illustrating the CODH 1 modified and Ru dye-sensitised TiO_2 NPs photoactive system. Reprinted with permission from ref. 176. Copyright 2010 American Chemical Society.

14502 | *J. Mater. Chem. A*, 2015, **3**, 14487–14516

This journal is © The Royal Society of Chemistry 2015

presence of potential gas phase reduction products such as light alkanes and alkenes.

As a conductive electron reservoir, carbon is also effective in channelling photoinduced electrons away from a photoactive host, thereby increasing the probability that photoexcited electrons reduce CO_2 rather than recombining with holes. Ong *et al.* reported a hybrid catalyst, composed of CNTs grown on a Ni impregnated TiO_2 composite, for CO_2 photoreduction to CH_4 under visible light.[185] The authors first deposited 10 wt% Ni onto commercial anatase *via* precipitation in the presence of glycerol. Carbon NTs were subsequently grown over the calcined Ni/TiO_2 through chemical vapour deposition. The band gap of the resulting hybrid material was 2.22 eV, significantly smaller than that of anatase TiO_2 (3.32 eV). Hence CNT incorporation served to narrow the band gap and improve visible light absorption in the hybrid catalyst. Visible light irradiation under water vapour revealed the $CNT/Ni/TiO_2$ hybrids were superior to either Ni/TiO_2 or pure anatase TiO_2, although progressive deactivation occurred after 4.5 h irradiation at which point CO_2 photoreduction activity was maximal. Photoactivity of the $CNT/Ni/TiO_2$ hybrid catalyst originated from improved visible light absorption and the excellent electron storage and transfer properties of the CNTs which helped to suppress electron–hole recombination.

Graphene, a two-dimensional planar structure of sp2 hybridised carbon, has received much attention in regard to photocatalytic applications for H_2 evolution,[58,163,186–194] photocurrent generation,[190,194–198] and dye degradation,[90,144,145,163,189,199–201] due to its outstanding electronic properties.[144,197] Graphene also offers extremely high specific surface areas[202] in excess of 2600 m^2 g^{-1}, a good CO_2 and H_2 adsorption capacity,[203,204] and has been reported to sensitise large band gap semiconductors for visible light photoabsorption.[205–207] However, less work has been conducted into the integration of graphene with photoactive materials for CO_2 photoreduction. Nevertheless, it is known that graphene oxide (GO), an unreduced form of graphene, despite being a poor electrical conductor,[195] is capable of photoreducing CO_2 to CH_3OH.[208] Liang *et al.* demonstrated that the photocatalytic activity of commercial P25 is greatly enhanced for CH_4 formation under both UV and visible light irradiation when used in conjunction with a low defect density, solvent-exfoliated graphene (SEG), compared to that achievable over defective, solvent-reduced graphene oxide (SGRO).[206] The

photoactivities of these SEG–P25 and SRGO–P25 composite films, which were synthesised by blade-coating a physical mixture of different amounts of graphene and P25 ink and subsequent annealing, are shown in Fig. 21a. Note that under UV illumination the presence of SGRO exerted little impact upon the photoactivity of TiO_2, whereas graphene possessing a low defect density exhibited better electrical mobility and concomitant superior photocatalytic efficiency under either UV or visible light.

Despite the popularity of graphene-derived materials, a direct comparison between graphene and its carbon nanotube (CNT) allotrope has not been well-explored. Further work by Liang *et al.* extended their studies on CO_2 photoreduction catalysed by blade-coated films to examine the integration of titania nanosheets (TiNS) with SEG or single-walled carbon nanotubes (SWCNT) to form either a two-dimensional graphene–titania nanosheet composite, or a one/two-dimensional carbon nanotube–titania nanosheet composite, respectively.[209] Fig. 21b shows that the SEG–TiNS composites outperformed SWCNT–TiNS in photoreducing CO_2 to CH_4 under UV irradiation. Conversely, composites of SWCNT–TiNS demonstrated better photoactivity under visible light illumination. It was proposed that the two-dimensional interface between SEG and TiNS facilitated intimate electronic and physical coupling relative to the one-/two-dimensional interface within the SWCNT–TiNS composite. Consequently, interfacial electron transfer from TiNS to SEG was greatly improved, inhibiting the recombination of photogenerated electron–hole pairs. In contrast, the better visible light photoactivity from SWCNT–TiNS was proposed to originate from the increased optical absorption of the SWCNT component at longer wavelengths relative to that of SEG. Accordingly, it was proposed that under visible light irradiation, photoinduced electrons generated at the SWCNT

Fig. 21 Methane formation rate of (a) SEG–P25 and SRGO–P25 films under UV and visible light illumination, and (b) SEG–TiNS and SWCNT–TiNS films under UV (100 W Hg vapour lamp, 365 nm) and visible light irradiation (natural daylight bulb, ~400 to 850 nm). Reprinted with permission from ref. 206 and 209. Copyright 2011 and 2012 American Chemical Society.
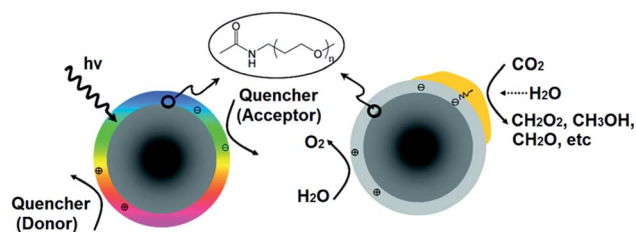

Fig. 20 PEG-functionalised carbon nanoparticles undergoing radiative recombination (left) and noble metal-coated & PEG-functionalised carbon nanoparticles photoreducing CO_2 (right). Reprinted with permission from ref. 184. Copyright 2011 American Chemical Society.
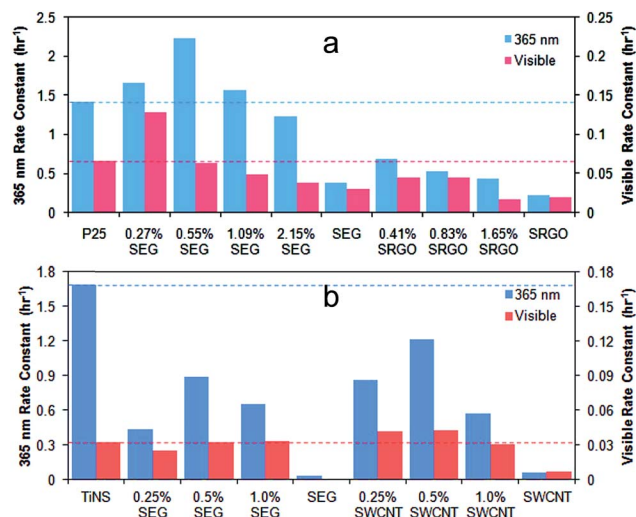
surface were transferred to the TiNS substrate for subsequent CO_2 photoreduction.

A series of graphene–Ta_2O_5 composites, with different loadings of the carbon, were prepared by Lv et al. through a hydrothermal route.[207] Impregnation with a Ni/NiO co-catalyst activated these composites for CO_2 photoreduction to CH_3OH and H_2 under UV-Vis illumination under aqueous conditions. Composites with 1 wt% graphene exhibited the highest photo-activity; in CO_2-aerated water the composite produced 3.4 times and 2.3 times the amount of CH_3OH and H_2 respectively than achieved over pure Ta_2O_5. This enhanced photocatalysis was attributed to the benefits of the graphene support in promoting effective interfacial charge transfer, as illustrated in Fig. 22. Photoinduced electrons generated at the Ta_2O_5 surface could be effectively transported to the surfaces of either graphene or the Ni/NiO dopant for subsequent transfer and CO_2 reduction.

Unlike the preceding materials, wherein as-synthesised graphene nanosheets were integrated with semiconductor particles through a simple impregnation/adsorption process, Tu et al. followed an alternative approach to prepare hollow spheres of alternating titania and graphene nanosheets for CO_2 photoreduction.[210] Fig. 23 shows how the surface of a poly(methyl methacrylate) (PMMA) template was first modified with a cationic polyelectrolyte, e.g. polyethylenimine (PEI) which electrostatically attracted negatively charged $Ti_{0.91}O_2$ nanosheets onto their surface. Subsequent surface modification of these titania-coated PMMA beads with PEI facilitated coating by negatively charged graphene oxide (GO) nanosheets. This process was repeated multiple times to thereby prepare a PMMA core composite with five alternating layers of $(PEI/Ti_{0.91}O_2/PEI/GO)_5$. Subsequent microwave treatment under an Ar environment decomposed the PMMA template, removed the PEI moiety, and reduced the GO to graphene (G). TEM (Fig. 23b and c) revealed that these $Ti_{0.91}O_2$ and graphene nanosheets alternated in a parallel, ordered lamellar arrangement, with a repeat distance estimated to be around 1.15 nm. Catalytic screening
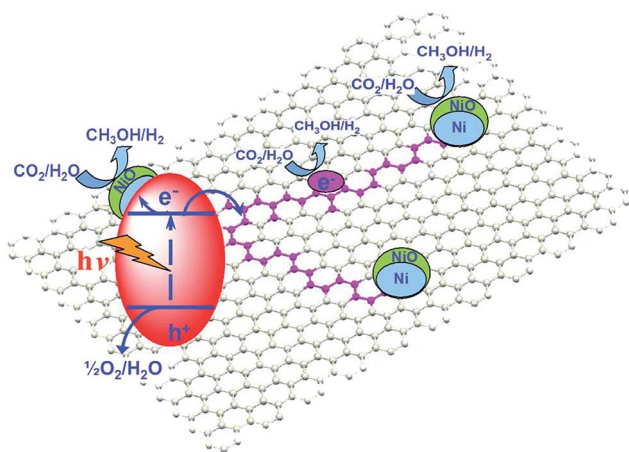
under UV-Vis illumination showed that the $(G/Ti_{0.91}O_2)_5$ hollow spheres were superior for CO_2 photoconversion versus $(Ti_{0.91}O_2)_5$ hollow spheres (synthesised without GO) and P25 titania in a glass reactor filled with CO_2 at ambient pressure, albeit the principal photolysis product was CO not CH_4. A number of explanations for the excellent behaviour of these $(G/Ti_{0.91}O_2)_5$ hollow composites were advanced. The ultrathin nature of the $Ti_{0.91}O_2$ nanosheets likely drove rapid transfer of charge carriers to active sites, increasing the probability of the photogenerated electrons participating in subsequent photoreduction chemistry; the compact stacking of $Ti_{0.91}O_2$ and graphene nanosheets would allow efficient interfacial electron transfer from the $Ti_{0.91}O_2$ to graphene layers, this spatial separation increasing the lifetime of photoexcited electrons. Hollow composite cores may also trap and multiply scatter incident photons, thereby improving light absorption and quantum efficiency.

Reduced graphene oxide (RGO) has also been employed within unique heterostructured optoelectronic materials, in which "tree"-like three-dimensional hierarchical titania nano-rods,[211] or one dimensional ZnO nanorods[212] (as wide-band-gap UV absorbing semiconductors) are contacted with CdS visible light sensitising nanoparticles via a suspended, RGO film. The resulting architectures ensure precise spatial localisation of each component and tunable charge-transport properties, facilitating a 100–150 % increase in the associated photocurrent density relative to the metal oxide/chalcogenide system alone, and 25% increase in methylene blue decomposition (ZnO/RGO/CdS), and 240% increase in the applied bias to photoelectrochemical hydrogen generation efficiency for hydrogen production via water-splitting (TiO_2/RGO/CdS).

2.3. Co-catalysts and plasmonic photocatalysts

Co-catalysts, typically Platinum Group and noble metals, are frequently deposited on semiconductor surfaces in order to (i) maximise the lifetime of photogenerated charge carriers, (ii) to activate reactants, and (iii) to improve the absorption of incident light.[213–216] Noble metals such as Au and Ag have lower Fermi levels than their partnered semiconductors, and hence can act as electron sinks that accept photoexcited electrons,[217,218] thereby retarding electron–hole recombination and

Fig. 22 Schematic of potential pathways for the transport of photo-induced electrons from a Ta_2O_5 semiconductor nanoparticle to active CO_2 photoreduction sites mediated by graphene. Reproduced from ref. 207 with permission from The Royal Society of Chemistry.
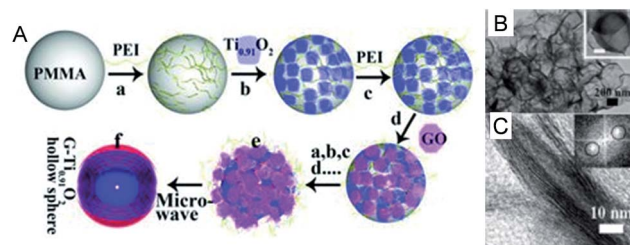
Fig. 23 (A) Stepwise preparation of alternating TiO_2 and graphene nanosheet hollow sphere assemblies, (B) TEM and (C) and HR-TEM images of $(G–Ti_0O_2)_5$ hollow spheres. Scale bar of the inset in (c): 100 nm. Inset in (C) is the fast Fourier Transform pattern of the ordered lamellar structures exhibited by the $(G–Ti_{0.91}O_2)_5$ hollow spheres. Reproduced with permission from ref. 210. Copyright 2012 Wiley.

14504 | J. Mater. Chem. A, 2015, **3**, 14487–14516

This journal is © The Royal Society of Chemistry 2015

increasing the availability of electrons for CO_2 photoreduction. It is generally held that, when co-catalysts are employed, photoconversion efficiency varies with the co-catalyst particle size, in turn usually governed by the method of their incorporation,[75,157,219] albeit the nature of this relationship (proportional or inversely proportional), magnitude and origin remains poorly studied and understood.

Recent work by Iizuka *et al.* has shown that the photoactivity of plate-like $ALa_4Ti_4O_{15}$ (A = Ca, Sr, and Ba) layered perovskites impregnated with a Ag co-catalyst varies with the method of co-catalyst loading.[75] Silver modification of $ALa_4Ti_4O_{15}$ with a $AgNO_3$ precursor was achieved *via*: (i) wet impregnation followed by H_2 reduction; (ii) *in situ* photodeposition; or (iii) liquid phase reduction using $NaPH_2O_2$. Under UV illumination and water, all these Ag-loaded $ALa_4Ti_4O_{15}$ materials were active in photoreducing CO_2 into CO predominantly, and a small amount of HCOOH, accompanied by H_2 and O_2 evolution, under a constant CO_2 flow rate of 15 mL min^{-1}. Ag loaded by liquid phase reduction demonstrated the highest photoactivity, followed by that through impregnation/H_2 reduction, ahead of those photodeposited. When photodeposition was employed, Ag NPs of around 30–40 nm populated edges of the as-prepared $BaLa_4Ti_4O_{15}$, while liquid phase reduction resulted in a homogeneous dispersion of <10 nm nanoparticles over the layered perovskite. Materials prepared *via* impregnation/H_2 reduction produced large aggregates of ~50 nm Ag particles, although some 10–20 nm Ag particles were observed at the edges of impregnated/reduced samples after photolysis. The basal plane and edges of plate-like $BaLa_4Ti_4O_{15}$ were suggested as the respective active sites for photooxidation and photoreduction. Accordingly, Ag deposited at the basal plane may undergo photodissolution and redeposition at the semiconductor edges during photocatalysis, with the particle size of such redeposited Ag dependent upon the concentration of dissolved silver ions. Consequently, *in situ* photolysis modified the Ag particle size to increase in the order: liquid phase reduction < impregnation/H_2 reduction < photodeposition. It was concluded that the photoactivity of Ag/$BaLa_4Ti_4O_{15}$ varied inversely with Ag particle size, a function of the co-catalyst incorporation route.

TiO_2 NTs arrays promoted by ultrafine Pt NPs, uniformly deposited *via* a rapid, microwave-assisted solvothermal approach, were investigated by Feng and co-workers.[220] In this method, the crystalline nanotube arrays were first loaded in a Teflon reaction chamber containing a 0.15 M H_2PtCl_6/CH_3OH solution. After an overnight immersion process, the reaction chamber was rapidly heated to 120 °C and held for 20 min before cooling. The resulting Pt/TiO_2 NTs arrays were isolated, washed and dried prior to catalytic testing. Dark field (S)TEM shown in Fig. 24a highlights the uniform distribution of Pt NPs (with an average diameter of 3.4 nm) across the TiO_2 NTs arrays. While such wet impregnation is simple to conduct and yields small Pt NPs, they exhibited a broad size distribution spanning 1.8–4.9 nm. Nevertheless, under irradiation by a solar simulator and water vapour, these Pt/TiO_2 NTs arrays were superior to unpromoted TiO_2 NTs arrays in photoreducing CO_2 to CH_4 and trace C_2H_6 at 45 °C. The excellent photoactivity of Pt/TiO_2 NTs arrays was attributed to the high Pt nanoparticle dispersion

(and hence density of surface active sites), coupled with efficient electron diffusion properties through the nanotube arrays.

In contrast, Wang *et al.* utilised a unique gas phase technique, tilted-target sputtering (TTS), to deposit size-controlled ultrafine Pt NPs onto a single crystalline titania thin film comprised of 1-D TiO_2 columns.[51] TTS enables precise control over both the flux of sputtered metal atoms and their radial distribution. Locating the TiO_2 film in the outer region of the deposition flux zone, where low energy atoms participate in nanoparticle formation, permitted the selective growth of ultrafine Pt NPs on the semiconductor surface as shown by TEM in Fig. 24b; Pt NPs with an average particle size of 1.04 ± 0.08 nm were uniformly coated on anatase TiO_2. It was claimed that such Pt NPs were preferentially deposited at surface defects on the titania substrate. While this gas-phase method necessitates high vacuum instrumentation, and hence is not readily scalable, it does offer Pt NPs possessing a narrow size distribution and tunable diameter (through varying the deposition time). The smallest and largest nanoparticles reported *via* this approach exhibited mean particle diameters of 0.63 ± 0.06 nm and 1.87 ± 0.31 nm, respectively (albeit a narrow range spanned). Subsequent exposure of Pt/TiO_2 catalyst films to water vapour and UV irradiation evidenced improved photoactivity compared with P25 and an analogous bare TiO_2 film for CO_2 photoreduction, forming predominantly CH_4 with trace CO under a slow CO_2 stream in a continuous flow reactor. Optimal photoactivity was achieved for a 1.04 ± 0.8 nm Pt/TiO_2 catalyst film, which delivered a remarkable combined quantum efficiency to CO and CH_4 of 2.41%. The observed photoactivity enhancement reflected a combination of the high surface area and single crystalline nature of the TiO_2 thin film, and excellent charge carrier separation characteristics conferred by the ultrafine Pt NPs. However, photocatalysis deteriorated after 5 h of irradiation, attributed to saturation of reactive sites by strongly-bound intermediate products, and consequent site-blocking.

Noble metals are often employed as co-catalysts to effect charge separation, but have been recently established to play an additional role as plasmonic photocatalysts in their own right, owing to the ability of gold and silver to absorb visible light through their localised surface plasmon resonance (LSPR).[96,145,221–225] This latter hot topic requires an
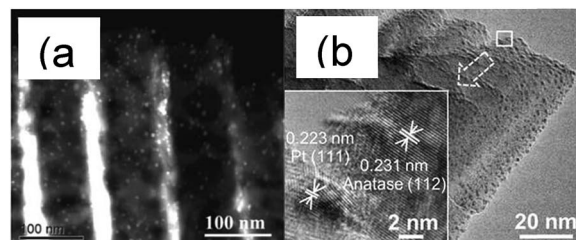
Fig. 24 (a) Dark field (S)TEM image of ultrafine Pt NPs deposited TiO_2 nanotube arrays,[220] and (b) TEM image of size resolved ultrafine Pt NPs on TiO_2 film. Inset: HRTEM image showing the lattice fringes corresponding to anatase TiO_2 (112) and Pt (111) NPs. Reproduced from ref. 157 with permission from The Royal Society of Chemistry.

This journal is © The Royal Society of Chemistry 2015

J. Mater. Chem. A, 2015, **3**, 14487–14516 | **14505**

understanding of the basic principles underlying the plasmonic phenomenon. The LSPR is a collective oscillation of free electrons within metal structures, established when the natural oscillation frequency of surface electrons (induced by charge density redistribution), resonates with the frequency of incident photons. The free electrons of plasmonic Au, Ag, and Cu nanostructures can be excited by the electromagnetic field of incident visible light; as the light wavefront impinges, the electron density is polarised across these metal nanostructures, such that free conduction electrons coherently oscillate in phase with the light, creating a dynamic dipole oscillator at the metal surface (Fig. 25).[225–227] Such intraband LSPR absorption (*e.g.* by Au 6sp electrons) induced by visible light is fundamentally different from the interband absorption caused by ultraviolet light (Au electrons excited from the 5d to 6sp bands).[228]

The strength and frequency of plasmon resonances depends on the size, shape, composition (for alloys) and local dielectric environment of the associated nanoparticles (see Fig. 26). These variations in LSPR peak positions and strengths strongly influence the photocatalytic capacities of such plasmonic nanomaterials.[215,230]

On the basis of the literature, at least three mechanisms have been proposed to account for the enhanced visible light photoactivity of noble metal/semiconductor plasmonic photocatalyts. First, it is hypothesised that visible light photoexcited electrons at the surface of the plasmonic metal can migrate across the metal–semiconductor interface into the conduction band of the associated semiconductor, or transferred directly to adsorbates, providing a source of localised, energetic reductants.[231] Second, the polarised electric field induced by the LSPR of metal NPs could enhance reactant activation over neighbouring supports by the interplay between the resonating electron cloud of the metal NPs and nearby adsorbates (polarisable or possessing polar functional groups). Finally, photoexcited electrons may not actually transfer from plasmonic metal NPs to adjacent semiconductors/reactants nor interact with them indirectly *via* field effects, but may rather liberate heat during relaxation of photoelectrons to their groundstate, thereby promoting thermal catalysis, although it has proven extremely difficult to qualitatively or quantitatively determine any such heating effect.[232] All these models account for an increase in the photoexcited electrons available for chemical reduction.[227]

Plasmon-enhanced CO_2 photoconversion has been recently reported,[233,234] exemplified by AgX : Ag (X = Cl or Br) plasmonic
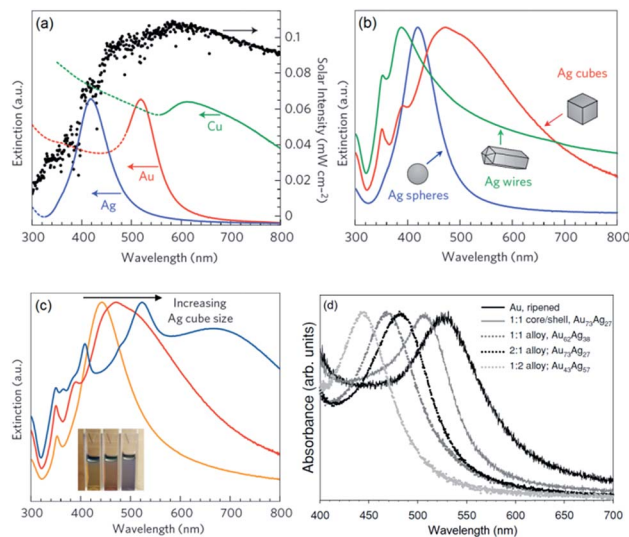
Fig. 26 The LSPR bands of plasmonic metal nanostructures with different shapes, sizes or compositions (for alloys): (a) nanoparticles of Au, Ag, and Cu; (b) Ag nanostructures with various shapes; (c) nanocubes of Ag with different cubic sizes; and (d) alloy of Au–Ag with different Au : Ag ratios. Reprinted by permission from Macmillan Publishers Ltd. Ref. 227, copyright 2011. Reproduced with permission from ref. 230. Copyright 2011 Wiley.

NPs synthesised through a glycerol-mediated precipitation route in the presence of polyvinylpyrolidone.[235] Despite their similar synthetic protocols, AgCl : Ag and AgBr : Ag exhibited cube-tetrapod-like and hexagonal nanoplates respectively. XPS and XRD confirmed the presence of metallic Ag on the as-prepared AgX : Ag NPs, with UV-Vis revealing significantly different band gaps of 3.95 (AgCl) and 3.45 eV (AgBr). When dispersed in $NaHCO_3$ aqueous medium under visible light, the AgX : Ag plasmonic photocatalysts were active for photoreducing CO_2 into CH_3OH, attributed to the metallic Ag LSPR influencing the contacted AgX : Ag NPs. Recycling experiments indicated that these plasmonic catalysts were stable under the screening conditions, although *in situ* Ag^+ reduction to additional silver metal is a plausible deactivation pathway following prolonged irradiation.

Hou *et al.* deposited islands of plasmonic Au NPs onto a sol–gel prepared TiO_2 thin film *via* electron beam evaporation.[148] Under visible light illumination and water vapour the resulting Au-promoted TiO_2 thin film exhibited a 24-fold activity enhancement relative to a bare TiO_2 thin film for CO_2 photoreduction to CH_4 in a stainless steel reactor at 75 °C. The low, but finite, photoactivity of the parent TiO_2 film was attributed to defect-induced, sub-band gap photoexcitation. Complementary calculations suggested that direct electron transfer from Au NPs to TiO_2 was not feasible under plasmonic excitation, and hence the superior photoactivity was ascribed to an increased sub-band gap charge carrier formation rate, indirectly induced by the LSPR of gold. Methane was the only reductant formed over the bare TiO_2 thin film under UV irradiation, however a range of products were formed over the Au/TiO_2 thin film wherein the production rate followed $CH_4 > C_2H_6 > HCHO > CH_3OH$.
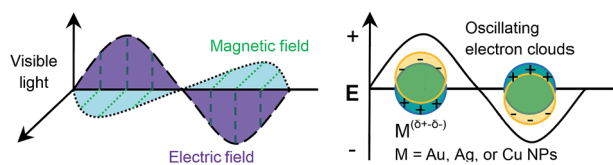

Fig. 25 Electromagnetic field of visible light interacting with plasmonic metal NPs: a dipole oscillator forms and resonates with the electromagnetic field of the incident visible light. Reproduced with permission from ref. 229.

14506 | J. Mater. Chem. A, 2015, 3, 14487–14516

This journal is © The Royal Society of Chemistry 2015

Surprisingly, the pure Au NPs were also reported to generate these aforementioned organic products, although the overall productivity was lower than that of the Au/TiO_2 composite. The photocatalytic activity of Au NPs was proposed due to interband electronic transitions (and not the LSPR) wherein electrons were photoexcited to a potential more negative than the TiO_2 conduction band and redox potential required to form desired reduction products. The synergy between Au NPs and the TiO_2 film under UV irradiation was attributed to improved charge carrier separation.

Small Cu and Ag NPs which exhibit plasmonic effects have also been successfully loaded onto TiO_2 nanorod films by an electrochemical method.[219,236] Tan et al. loaded Cu NPs onto a TiO_2 film via a 0.01 mM $CuSO_4$ and 0.1 M K_2SO_4 mixed electrolyte at a pulse potential of -0.8 V for between 0–300 s.[236] Under UV illumination and water, the resulting composite film (prepared at the optimum 100 s deposition time) demonstrated superior activity to a bare TiO_2 or P25 film in photoreducing CO_2 into CH_4. The copper co-catalyst benefits were again ascribed to efficient charge separation due to plasmonic effects. However, it was reported that surface oxidation of Cu NPs to copper oxide occurred during photocatalyic screening. An electrochemical deposition method known as the double-potentiostatic method was also used to deposit Ag NPs onto a TiO_2 nanorod film.[219] This method favoured the formation of uniform and dense metallic nanoparticles due to quick nucleation and slow nanoparticle growth at high potential and low precursor concentration. Accordingly, Kong et al. loaded silver onto a TiO_2 film employing a 0.1 M KNO_3/0.2 mM sodium citrate/0.05 mM $AgNO_3$ electrolyte at nucleation potentials from -1.4 V to -0.8 V for 100 s, followed by a growth potential of -0.2 V for 2400 s. TiO_2/Ag films prepared at the optimum nucleation potential of -1.0 V exhibited improved photo-activity relative to a bare TiO_2 film in photoreducing CO_2 into CH_4 under UV illumination and water vapour. Photocatalytic performance was again postulated to arise from efficient charge separation due to silver plasmonic effects. Moreover, alloy or bimetallic plasmonic nanostructures, such as Au–Pt (as shown in Fig. 27a)[237] and Ag–Pt (as shown in Fig. 27b),[233] have also been discovered to enhance CO_2 the photoreduction by titania. In both cases, the introduction of plasmonic Au or Ag particles increased photocatalytic efficiency in terms of product selectivity and/or yield, ascribed to the LSPR effect of Au (Ag) NPs significantly increasing light absorption and charge separation of the photoexcited titania. Co-deposition of Au/Pt on TiO_2 NFs considerably enhanced photocatalytic activities for both H_2 generation and CO_2 reduction compared to singly decorated (Pt/TiO_2 or Au/TiO_2) fibres. Bijith and co-workers' study demonstrates that Ag, Pt and bimetallic Ag–Pt NPs enable CH_4 and CO product selectivity to be tuned:[233] product yields were enhanced more than seven-fold compared with native TiO_2, with a high CH_4 selectivity. This was attributed to the enhanced availability of photoexcited electrons via improved electron–hole pair generation, and surface trapping of photo-excited electrons within the titania lattice, enabling the necessary accumulation of charge to drive the eight-electron CH_4 forming process from adsorbed CO_2.

2.4. Miscellaneous photocatalysts

Cationic and/or anionic doping is commonly employed to decrease semiconductor band gaps.[238–242] Richardson et al. co-doped TiO_2 with Cu and Ga via a sol–gel route to form composites that were active in CO_2 photoreduction at longer wavelengths than possible utilising P25.[139] The absorption band edge wavelength of doped photocatalysts increased in the order P25 < Ga/TiO_2 < Cu/TiO_2 < Cu, Ga/doped TiO_2, with a corresponding decrease in the band of the doped-materials relative to P25. It should be noted that the absorption band edges of doped materials still resides in the UV region despite their modified optical properties. Under 200 W near-UV (350–450 nm), 350 W mid-UV (280–350 nm) or 500 W deep-UV (240–260 nm) irradiation, and immersion in a NaOH and $KHCO_3$
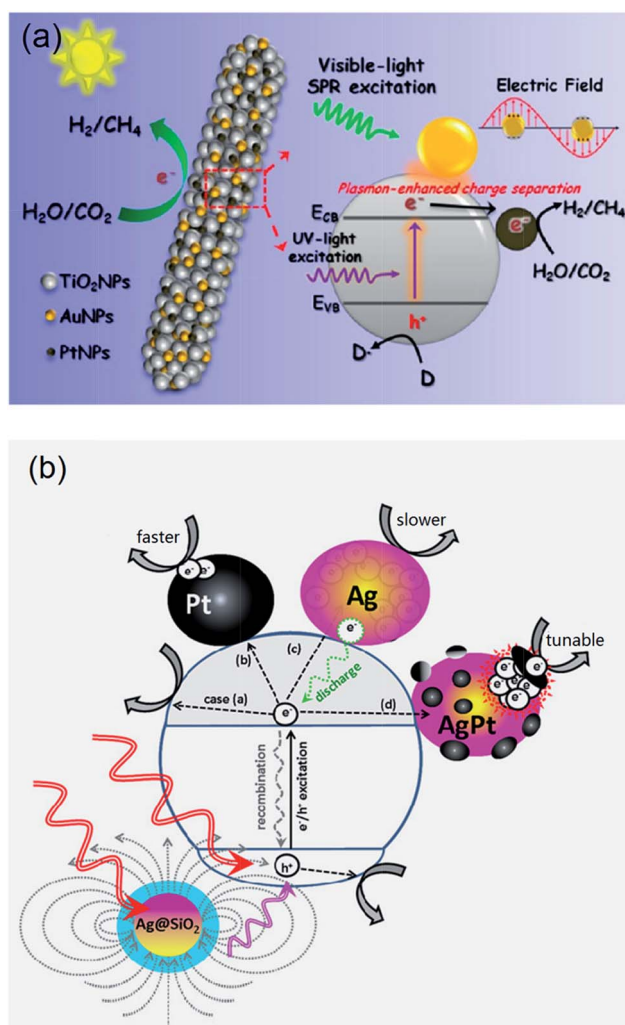
Fig. 27 (a) Illustration of the photocatalytic process to produce H_2 and to reduce CO_2 over $Au/Pt/TiO_2$ NFs. Reprinted with permission from ref. 237. Copyright 2010 American Chemical Society. (b) Illustration of different photoexcited charge pathways following electron–hole generation assisted by plasmonic nanoparticles over core–shell $Ag@SiO_2$: transfer to the [a] semiconductor surface, [b] Pt NP surface, [c] Ag NP surface, and [d] bimetallic Ag–Pt surface. Reproduced with permission from ref. 233. Copyright 2013 IOP Publishing Ltd.

Table 2 Photocatalytic reaction conditions and CO_2 reduction performance of exemplar nanostructured materials

Material	Light source	$T/^{\circ}C$	P_{CO_2}/bar	Product yield/$\mu mol\ h^{-1}\ g_{cat}^{-1}$	Selectivity (product)/mol%	Quantum efficiency/%	Reference
ZnGa$_2$O$_4$	300 W Xe	—	1	1 wt% RuO$_2$ 7245, mesoporous 762	100 (CH$_4$)	—	113
Pt/TiO$_2$	400 W Xe (20 mW cm^{-2} 250–388 nm)	22–32	1	1361 (CH$_4$), 180 (CO)	88.5 (CH$_4$), 11.5 (CO)	2.33 (CH$_4$)0.077 (CO)	51
Zn$_2$SnO$_4$	300 W Xe	—	1	Bulk 17.0 (CH$_4$), atactic 34.5, micro-octahedra 54.6, nanoplate/micro-octahedra 288.9, RuO$_2$/Pt 1246.3	100 (CH$_4$)	—	155
W$_{18}$O$_{49}$	300 W Xe(30 mW cm^{-2})	70	1	11.31 (CH$_4$, visible) 858 (CH$_4$, UV-visible)	95 (CH$_4$), 5 (ethanol, acetone…)	0.03 (CH$_4$, visible)	65
Au/Pt–TiO$_2$	500 W Xe	—	—	114 (CH$_4$), 20 (CO)	85 (CH$_4$),15 (CO)	—	234
(RuO$_2$ + Pt)–Zn$_2$GeO$_4$	300 W Xe	RT	1	25	100 (CH$_4$)	—	94
Nafion layer-enhanced Pd–TiO$_2$	300 W Xe (λ > 300 nm)	—	—	21.9 (CH$_4$), 1.03 (C$_2$H$_6$)	95.5 (CH$_4$), 4.5 (C$_2$H$_6$)	—	170
Pt–Cu/TiO$_2$	200 W Xe (320–780 nm)	50	2	9.8 (CH$_4$), 5.9 (CO), 51 (H$_2$)	14.7 (CH$_4$), 8.8 (CO)	—	249
0.5 wt% Cu/TiO$_2$–SiO$_2$	Xe (2.4 mW cm^{-2} 250–400 nm)	—	—	10 (CH$_4$), 60 (CO)	14.3 (CH$_4$), 85.7 (CO)	0.56 (CH$_4$), 0.85 (CO)	121
0.5 wt% Pt ZnAl$_2$O$_4$–ZnGaNO	300 W Xe (λ ≥ 420 nm)	—	1	9.2	100 (CH$_4$)	—	111
0.5 wt% Pt/NaNbO$_3$	300 W Xe (λ > 300 nm)		0.8	0% cubic 2.19 (CH$_4$), 15 (CO), 45 (H$_2$), 69% cubic 5.86 (CH$_4$), 16 (CO), 42 (H$_2$), 98% cubic 4.91 (CH$_4$), 12 (CO), 25 (H$_2$)	12.7 (CH$_4$), 87.3 (CO), 26.8 (CH$_4$), 73.2 (CO), 29 (CH$_4$) 71 (CO)	—	250
AgBr/TiO$_2$	150 W Xe (λ > 420 nm)	RT	75	5.71 (CH$_4$), 15.57 (CH$_3$OH), 2.66 (C$_2$H$_5$OH), 6.43 (CO)	18.8 (CH$_4$) 51.3 (CH$_3$OH) 8.8 (C$_2$H$_5$OH)	—	163
Amine-functionalised TiO$_2$	Xe (λ > 302)	—	—	3.08 (CH$_4$), 11.92 (CO)	20.5 (CH$_4$), 79.5 (CO)	—	67
Pt–, Au–, or Ag–TiO$_2$	350 W Xe (35 mW cm^{-2})	60	—	0.2% Pt 2.85, 0.2% Au 1.51, 0.1% Ag 0.65, TiO$_2$ 0.238	100 (CH$_4$)	0.68,0.36, 0.15, 0.06	123
Ti$_{0.91}$O$_2$	300 W Xe	—	1	Graphene 1.14 (CH$_4$), 8.91 (CO), Ti$_{0.91}$O$_2$ 1.41 (CH$_4$)	11.4 (CH$_4$), 88.6 (CO), 100 (CH$_4$)	—	210
Cu(I) dye-sensitised TiO$_2$	300 W Xenon (λ > 420 nm)	—	1	0.725	100 (CH$_4$)	—	174
Ga$_2$O$_3$	300 W Xe (500 mW cm^{-2})	—	—	0.3935	100 (CH$_4$)	0.007	107
RuO$_2$–Zn$_2$GeO$_4$	300 W Xe	—	1	0.39 (CH$_4$), 1.01 (CO)	25.5 (CH$_4$), 74.5 (CO)	—	97
Carbon nanotubes@ Ni/TiO$_2$	75 W visible daylight lamp (λ > 400 nm)	50	1	0.145	100 (CH$_4$)	—	185
Pd–TiO$_2$	500 W Hg (λ > 310 nm)	5	0.867	1% Pd 0.037 (CH$_4$), 0.06 (C$_2$H$_6$), 0.04 (CO), TiO$_2$ 0.027 (CH$_4$), 0.353 (CO)	78.9 (CH$_4$), 12.7 (C$_2$H$_6$), 8.4 (CO), 7.1 (CH$_4$), 92.9 (CO)	—	68
N-doped ZnO	8 W fluorescent tube 7 mW cm^{-2}	50	2	0.01 (CH$_4$), 0.03 (CH$_3$OH), 0.04 (CO), 0.09 (H$_2$)	4.8 (CH$_4$), 19.0 (CH$_3$OH), 23.8 (CO)	—	112
CdS/TiO$_2$, Bi$_2$S$_3$/TiO$_2$	500 W Xe (λ ≥ 400 nm)	—	1	CdS 40.1, TNTs–CdS 32.2,Bi$_2$S$_3$ 64.5, TNTs–Bi$_2$S$_3$ 45.3, TNTs 20.5, P$_{25}$ 18.2	100 (CH$_3$OH)	—	165
Graphene-modified NiO$_x$–Ta$_2$O$_5$	400 W Metal halogen lamp	RT	1	52 (CH$_3$OH), 41 (H$_2$)	55.9 (CH$_3$OH)	—	207
AgCl : Ag, AgBr : Ag	300 W Xe, (λ ≥ 400 nm)	0	1	AgCl 37.7, AgBr 21.7	100 (CH$_3$OH)	1.3 0.97	235
Bi$_2$WO$_6$	300 W Xe (λ ≥ 420 nm)	0	—	Hollow microspheres 16.3, bulk 0.64	100 (CH$_3$OH)	—	157

14508 | J. Mater. Chem. A, 2015, 3, 14487–14516

This journal is © The Royal Society of Chemistry 2015

Table 2 (*Contd.*)

Material	Light source	$T/^\circ$C	P_{CO_2}/bar	Product yield/μmol h^{-1} g$_{cat}^{-1}$	Selectivity (product)/mol%	Quantum efficiency/%	Reference
g-C_3N_4	300 W Xe ($\lambda \geq$ 420 nm, 267 mW cm^{-2})	20	1.013	u-g-C_3N_4 6.28 (CH_3OH), 4.51 (C_2H_5OH), 21.33 (O_2), m-g-C_3N_4 3.64 (C_2H_5OH), 10.29 (O_2), trace (CH_3OH)	19.6 (CH_3OH), 14 (C_2H_5OH), 26.1 (C_2H_5OH)	0.04 (CH_3OH + C_2H_5OH), 0.018 (C_2H_5OH)	120
TiO_2	500 W Xe ($\lambda >$ 300 nm, 2.5 mW cm^{-2})	—	1	Anatase-brookite 0.59, flower-like rutile 0.32, rutile 0.30, anatase 0.19, P_{25} 0.18	100 (CH_3OH)	0.0059, 0.0032, 0.0030, 0.0019, 0.0018	79
FeTiO$_3$/TiO$_2$	500 W Xe ($\lambda >$ 300 nm)	—	—	TiO_2 0.175 (UV-visible), 10% FeTiO$_3$/TiO$_2$ 0.338 (UV-visible), 20% FeTiO$_3$/TiO$_2$ 0.462 (UV-visible), 50% FeTiO$_3$/TiO$_2$ 0.298 (UV-visible), TiO$_2$ 0.141(visible), 10% FeTiO$_3$/TiO$_2$ 0.319 (visible), 20% FeTiO$_3$/TiO$_2$ 0.432 (visible), 50% FeTiO$_3$/TiO$_2$ 0.352 (visible)	100 (CH_3OH)	—	166
ZIF-8/Zn$_2$GeO$_4$	500 W Xe	—	—	Zn$_2$GeO$_4$ 0.14 (CH_3OH), Zn$_2$GeO$_4$/ZIF-8 0.23 (CH_3OH), 1 wt% Pt/Zn$_2$GeO$_4$/ZIF-8 0.27 (CH_3OH)	100 (CH_3OH)	—	95
Graphene oxide (GO)	300 W halogen lamp	25	—	GO-3 0.172, GO-1 0.110, GO-2 0.089	100 (CH_3OH)	—	208
Zn–Cu–M(III) (M = Al, Ga) layered double hydroxides	500 W Xe (UV-visible)	32–40	0.023	[Zn$_{1.5}$Cu$_{1.5}$Ga(OH)$_8$]$^{2+}$ 0.17 (CH_3OH), 0.079 (CO)[Zn$_3$Ga(OH)$_8$]$^{2+}$ 0.051 (CH_3OH), 0.080 (CO), [Zn$_3$Al(OH)$_8$]$^{2+}$ 0.039 (CH_3OH), 0.62 (CO),[Zn$_{1.5}$Cu$_{1.5}$Al(OH)$_8$]$^{2+}$ 0.13 (CH_3OH), 0.37 (CO)	68.3 (CH_3OH), 31.7 (CO), 38.9 (CH_3OH), 61.1 (CO), 5.9 (CH_3OH), 94.1 (CO), 26 (CH_3OH), 74 (CO)	0.00015 (CH_3OH), 0.000019 (CO), 0.00028 (CH_3OH), 0.000083 (CO), —	134
Ag/ALa$_4$Ti$_4$O$_{15}$ (A = Ca, Ba and Sr)	400 W Hg	RT	1	Ca 4.3 (HCOOH), 3.3 (CO), 18.7 (H$_2$), 7.0 (O$_2$), Ba 10 (HCOOH), 14.3 (CO), 33.3 (H$_2$), 23.3 (O$_2$), Sr 16.7 (HCOOH), 6.0 (CO), 9.0 (H$_2$), 6.0 (O$_2$)	HCOOH: 12.9, CO: 9.9, HCOOH: 82.3, CO: 17.7, HCOOH: 44.3, CO: 15.9	—	75
BiVO$_4$	300 W Xe ($\lambda \geq$ 400 nm, or without UV filter)	0	1	Monoclinic BiVO$_4$ 110 (visible), tetragonal BiVO$_4$ 12.5 (visible), monoclinic BiVO$_4$ 2150 (UV-visible), tetragonal BiVO$_4$ 250 (UV-visible)	100 (C_2H_5OH)	—	77
Dye-sensitised + dehydrogenase TiO$_2$	Halogen lamp ($\lambda >$ 420 nm 45 mW cm^{-2})	20	—	287.2	100 (CO)	—	176
KTaO$_3$ by SSR or solvothermal	300 W Xe	—	—	SSR–KTaO$_3$ 0.436 (H$_2$), 0.041 (CO), 0.173 (O$_2$), hexane–KTaO$_3$ 0.088 (CO), 40.13 (H$_2$), 0.4 (O$_2$), ethanol–KTaO$_3$ 0.283 (CO), 84.7 (H$_2$), 0.2 (O$_2$)	6.3 (CO), 0.2 (CO), 0.6 (CO)	—	74

aqueous medium, Cu and Ga co-doped TiO_2 photocatalysts were superior to P25 and the monometal-doped titanias in photoreducing CO_2 to HCOOH and other carbonic products (determined by TOC) in a continuous flow reactor at room temperature. Highest photoactivity was observed for the $Cu_{0.78}$–$Ga_{0.22}/TiO_2$ catalyst, with Cu the proposed CO_2 adsorption and reduction site for HCOOH and other organic products which include trace CH_3OH and HCHO.

Anion doping by Tsai et al. improved the visible light absorption properties of $InTaO_4$. Doping was performed by nitridation of SSR prepared $InTaO_4$ under flowing NH_3 at 800 °C,[243] resulting in the absorption band edge shifting to longer wavelengths in comparison to pure $InTaO_4$. Results were attributed to hybridisation between the N 2p and O 2p orbitals, which shifts the valence band upwards, thereby narrowing the $InTaO_4$ band gap. Under visible light illumination (390 to 770 nm) and in the presence of water, the prepared N-doped $InTaO_4$ outperformed pure $InTaO_4$ in photoreducing CO_2 into CH_3OH in a continuous flow reactor. XANES analysis indicated that N doping narrowed the band gap, and induced oxygen vacancies, the latter possibly contributing to photocatalytic enhancement. The photoactivity of the N-doped $InTaO_4$ was further improved by the addition of a Ni@NiO core–shell co-catalyst, incorporated through a sequence of wet impregnation, chemical reduction and final calcination. Promotion by the Ni@NiO core–shell co-catalyst was ascribed to enhanced charge separation and light harvesting.

Solid solutions formed between wide and narrow band gap semiconductors have been reported to possess valence and conduction bands that provide smaller gaps than their parent materials.[244–247] In general, the component semiconductors must possess the same crystal structure and similar lattice parameters. Liu et al. recently reported the application of Cu_x-$Ag_yIn_zZn_kS_m$ solid solutions as visible light photocatalysts for CO_2 photoreduction.[248] The band gap of this composite was a strong function of composition, and spanned 1.33–1.44 eV. Visible light irradiation (1000 W Xenon lamp at $\lambda > 400$ nm) in a $NaHCO_3$ aqueous medium of these solid solution photocatalysts facilitated CO_2 photoreduction to CH_3OH in a closed glass gas circulation system. Systematic relations could not be derived between the catalyst composition and photoactivity, although photoactivity was composition dependent. A range of co-catalysts were investigated, including RuO_2 and $Rh_{1.32}Cr_{0.66}O_3$, although these did not promote CO_2 conversion. Methanol productivity was enhanced under a H_2 environment, wherein a higher density of protons was formed.

3. Conclusions and future directions

A wide variety of approaches have been developed for the synthesis of photocatalytically active materials for CO_2 reduction to solar fuels and chemicals. To date, there is no standard protocol for evaluating photocatalytic performance, or single parameter that enables quantitative benchmarking of CO_2 conversion efficiencies to specific carbon-containing solar fuels or chemicals. In a first step towards addressing these deficiencies, Table 2 compares a range of the nanomaterials discussed in this review, with a view to informing on which show the most promise with respect to productivity per unit catalyst mass, and thus provide a strong rationale for future development. Of course, many additional factors such as earth abundance, cost, toxicity, and scalability will also influence which materials are ultimately best suited to commercialisation. However, a step-change in photoactivity, and comprehensive mechanistic insight into the catalytic cycle and nature of the surface sites participating in CO_2 adsorption and reduction, is required before such considerations should influence ongoing fundamental research efforts.

The optoelectronic properties of crystalline materials, and hence their photoactivity, are a strong function of the crystal structure, with different semiconductor polymorphs exhibiting disparate photocatalytic behaviour reflecting their surface atom arrangement and attendant electronic band structure. Although surface defects may serve as electron–hole recombination centres detrimental to the achievement of high quantum efficiencies, such sites can also promote visible light absorption and hence photocatalysis. Band gap engineering of earth abundant, large band gap semiconductor to facilitate visible light photocatalysis remains an important barrier to visible light absorption properties, although transition metal and p-block dopants provide a simple route to band-gap narrowing. Integrated dyes or small band gap semiconductors may also be employed as visible light sensitisors of conventional semiconductor photocatalysts, with the resulting hybrid, composite materials facilitating both UV and visible light capture and efficient charge carrier separation via preferential transfer of photoexcited electrons into one material and of holes into the other. In the latter regard, one- and two-dimensional semiconductor nanostructures, exhibiting high surface to volume ratios, can promote efficient transport of charge carriers to adsorbates during photocatalysis.

Integration of photoactive semiconductors with electrically conductive materials such as graphene offers new routes to maximising charge carrier lifetimes and consequent electron transfer to CO_2. High surface area and porous materials increase the density of surface active sites available to chemically bind and activate CO_2, its reactive intermediates, and water. Such nanostrutures can be created through the synthesis of semiconductors with intrinsic porosity on the micro-, meso- or macroscale, or via immobilisation (embedding) of photocatalysts onto (within) an inert, high area architecture. Three-dimensional hierarchical materials epitomise catalyst engineering, affording rapid molecular transport to/from active sites, enhanced light harvesting, and superior charge carrier transport and recombination characteristics. It seems extremely unlikely that any single semiconductor composition or structure can deliver the requisite optical, material and catalytic properties necessary to harness sunlight under ambient conditions for the rapid and selective photoreduction of CO_2 into the key chemical targets of methane, methanol, formaldehyde or ethene, hence the majority of promising systems employ co-catalysts whose contributions depend strongly on their method of incorporation.

Noble metal co-catalysts in particular offer exciting possibilities for visible light absorption through plasmonic effects, and indeed have even proven efficient photocatalysts in their own right for the selective oxidation of CO, ethene and ammonia[251] and reduction of nitroaromatics.[252] Photoreactor design will play an increasingly important role in ensuring optimum light (and catalyst) utilisation for CO_2 reduction, and enable quantitative benchmarking of different photocatalysts in terms of their absolute productivity, selectivity and quantum efficiency. Innovation is required to facilitate CO_2 separation/recycle, on-stream gas/liquid product separation, and optical materials to avoid losses in transmission to the internal reactor volume.

Ultimately, the final selection and commercialisation of the most promising (i.e. highly active, selective and stable) photocatalysts will be dictated by process economics, since even the highest value oxygenate or olefin products directly derivable from CO_2 will continue to face stiff competition with low cost fossil fuel sources for the foreseeable future. Indicative 2015 prices per metric ton are: methanol $420; formaldehyde $420; formic acid $500, and ethylene/propylene $800–1100. Overall process costs will be a strong function of the choice of chemical precursors, type and recyclability of solvents, (re)use of textural templates, mechanothermal processing, photocatalyst forming, and reactor operating conditions (temperature, pressure, separation and recycle). Many of the most promising photocatalysts described in this review utilise noble metal co-catalysts,[40,51,94,123,161,213,220,234,249] and with common H_2PtCl_6 and $HAuCl_4$ prices in excess of $10 000 per kg, high turnover numbers per metal atom (>3000) would be essential to even recoup the precursor costs. An obvious target for synthetic improvement is thus maximising noble metal efficiency through e.g. lowering the size/dimensionality of associated nanostructures, or atomically dispersing noble metal atoms exclusively within the terminating layer of catalysts.[253–256] Soft and hard templating methods are widely adopted in heterogeneous catalysis to introduce porosity, and hence enhance the surface density and accessibility of active sites.[137] A number of photocatalysts for CO_2 reduction employ such templates to similar effect, typically surfactants (e.g. TTAB,[107] CTAB[77,163,164] and P123 (ref. 78 and 112)) or polymers.[210] While their costs are comparatively low ($150–350 per kg), in the majority of cases such surfactants are removed through combustion and hence are not recoverable, and even solvent-extraction protocols rarely recover sufficiently pure and chemically unaltered templates amenable to re-use, though ultrasonic template removal shows promise as an energy and atom efficient solution.[257] The majority of synthetic strategies for nanostructure photocatalysts employ solvothermal processing, and hence comparatively low (<200 °C) temperatures (in the absence of a template calcination step) offering little scope for cost savings via energy input reduction. As with all syntheses, Green Chemistry principles provide the best general guidelines to reduce the number of reaction steps and minimise associated waste generation and the use of auxiliaries,[258] in concert with lower production costs.

Reference

1 J. Barber and P. D. Tran, *J. R. Soc., Interface*, 2013, **10**, 20120984.

2 *Solar Fuels And Artificial Photosynthesis: Science And Innovation To Change Our Future Energy Options*, Royal Society of Chemistry, 2012, http://www.rsc.org/campaigning-outreach/global-challenges/energy/ (accessed June 1st, 2015).

3 D. Luthi, M. Le Floch, B. Bereiter, T. Blunier, J.-M. Barnola, U. Siegenthaler, D. Raynaud, J. Jouzel, H. Fischer, K. Kawamura and T. F. Stocker, *Nature*, 2008, **453**, 379–382.

4 C. John, N. Dana, A. G. Sarah, R. Mark, W. Bärbel, P. Rob, W. Robert, J. Peter and S. Andrew, *Environ. Res. Lett.*, 2013, **8**, 024024.

5 M. Z. Jacobson, *Energy Environ. Sci.*, 2009, **2**, 148–173.

6 T. Faunce, S. Styring, M. R. Wasielewski, G. W. Brudvig, A. W. Rutherford, J. Messinger, A. F. Lee, C. L. Hill, H. deGroot, M. Fontecave, D. R. MacFarlane, B. Hankamer, D. G. Nocera, D. M. Tiede, H. Dau, W. Hillier, L. Wang and R. Amal, *Energy Environ. Sci.*, 2013, **6**, 1074–1076.

7 United Nations, *The Future We Want: Outcome*, 2012, https://sustainabledevelopment.un.org/futurewewant.html (accessed June 1st, 2015).

8 M. T. Lin, A. Occhialini, P. J. Andralojc, J. Devonshire, K. M. Hines, M. A. J. Parry and M. R. Hanson, *Plant J.*, 2014, **79**, 1–12.

9 D. G. Nocera, *Acc. Chem. Res.*, 2012, **45**, 767–776.

10 H. Dau, C. Limberg, T. Reier, M. Risch, S. Roggan and P. Strasser, *ChemCatChem*, 2010, **2**, 724–761.

11 G. F. Moore and G. W. Brudvig, *Annu. Rev. Condens. Matter Phys.*, 2011, **2**, 303–327.

12 R. Lomoth, A. Magnuson, M. Sjödin, P. Huang, S. Styring and L. Hammarström, *Photosynth. Res.*, 2006, **87**, 25–40.

13 K. Maeda and K. Domen, *J. Phys. Chem. Lett.*, 2010, **1**, 2655–2661.

14 Y. Tachibana, L. Vayssieres and J. R. Durrant, *Nat. Photonics*, 2012, **6**, 511–518.

15 T. Hisatomi, J. Kubota and K. Domen, *Chem. Soc. Rev.*, 2014, **43**, 7520–7535.

16 M. Aresta and A. Dibenedetto, *Dalton Trans.*, 2007, 2975–2992.

17 J. Qiao, Y. Liu, F. Hong and J. Zhang, *Chem. Soc. Rev.*, 2014, **43**, 631–675.

18 C. Costentin, M. Robert and J.-M. Saveant, *Chem. Soc. Rev.*, 2013, **42**, 2423–2436.

19 N. Z. Muradov and T. N. Veziroglu, *Int. J. Hydrogen Energy*, 2005, **30**, 225–237.

20 G. A. Olah, *Angew. Chem., Int. Ed.*, 2005, **44**, 2636–2639.

This journal is © The Royal Society of Chemistry 2015

J. Mater. Chem. A, 2015, **3**, 14487–14516 | **14511**

21 G. A. Olah, G. K. S. Prakash and A. Goeppert, *J. Am. Chem. Soc.*, 2011, **133**, 12881–12898.

22 I. Ganesh, *Renewable Sustainable Energy Rev.*, 2014, **31**, 221–257.

23 A. Goeppert, M. Czaun, J.-P. Jones, G. K. Surya Prakash and G. A. Olah, *Chem. Soc. Rev.*, 2014, **43**, 7995–8048.

24 C. S. Song, *Catal. Today*, 2006, **115**, 2–32.

25 M. Taherimehr and P. P. Pescarmona, *J. Appl. Polym. Sci.*, 2014, **131**, 41141.

26 A. I. Cooper, *J. Mater. Chem.*, 2000, **10**, 207–234.

27 http://www.petrochemistry.eu/about-petrochemistry/facts-and-figures.html (accessed June 2nd, 2015).

28 T. Ren, M. Patel and K. Blok, *Energy*, 2006, **31**, 425–451.

29 Y. Xing, W. Xie, W. Fang, Y. Guo and R. Lin, *Energy Fuels*, 2009, **23**, 4021–4024.

30 G. Palmisano, V. Augugliaro, M. Pagliaro and L. Palmisano, *Chem. Commun.*, 2007, 3425–3437.

31 M. Halmann, *Nature*, 1978, **275**, 115–116.

32 T. Inoue, A. Fujishima, S. Konishi and K. Honda, *Nature*, 1979, **277**, 637–638.

33 B. R. Eggins, J. T. S. Irvine, E. P. Murphy and J. Grimshaw, *J. Chem. Soc., Chem. Commun.*, 1988, 1123–1124.

34 S. C. Roy, O. K. Varghese, M. Paulose and C. A. Grimes, *ACS Nano*, 2010, **4**, 1259–1278.

35 V. L. Kuznetsov and P. P. Edwards, *ChemSusChem*, 2010, **3**, 44–58.

36 A. Kubacka, M. Fernandez-Garcia and G. Colon, *Chem. Rev.*, 2012, **112**, 1555–1614.

37 H. Tong, S. Ouyang, Y. Bi, N. Umezawa, M. Oshikiri and J. Ye, *Adv. Mater.*, 2012, **24**, 229–251.

38 A. J. Morris, G. J. Meyer and E. Fujita, *Acc. Chem. Res.*, 2009, **42**, 1983–1994.

39 V. P. Indrakanti, J. D. Kubicki and H. H. Schobert, *Energy Environ. Sci.*, 2009, **2**, 745–758.

40 O. K. Varghese, M. Paulose, T. J. LaTempa and C. A. Grimes, *Nano Lett.*, 2009, **9**, 731–737.

41 M. Tahir and N. S. Amin, *Energy Convers. Manage.*, 2013, **76**, 194–214.

42 G. Liu, N. Hoivik, K. Wang and H. Jakobsen, *Sol. Energy Mater. Sol. Cells*, 2012, **105**, 53–68.

43 A. Dhakshinamoorthy, S. Navalon, A. Corma and H. Garcia, *Energy Environ. Sci.*, 2012, **5**, 9217–9233.

44 S. N. Habisreutinger, L. Schmidt-Mende and J. K. Stolarczyk, *Angew. Chem., Int. Ed.*, 2013, **52**, 7372–7408.

45 Y. Ma, X. Wang, Y. Jia, X. Chen, H. Han and C. Li, *Chem. Rev.*, 2014, **114**, 9987–10043.

46 A. Paracchino, V. Laporte, K. Sivula, M. Grätzel and E. Thimsen, *Nat. Mater.*, 2011, **10**, 456–461.

47 S. Ardo and G. J. Meyer, *Chem. Soc. Rev.*, 2009, **38**, 115–164.

48 A. D. Handoko, K. Li and J. Tang, *Curr. Opin. Chem. Eng.*, 2013, **2**, 200–206.

49 S. Y. Reece, J. A. Hamel, K. Sung, T. D. Jarvi, A. J. Esswein, J. J. H. Pijpers and D. G. Nocera, *Science*, 2011, **334**, 645–648.

50 S. Hu, M. R. Shaner, J. A. Beardslee, M. Lichterman, B. S. Brunschwig and N. S. Lewis, *Science*, 2014, **344**, 1005–1009.

51 W.-N. Wang, W.-J. An, B. Ramalingam, S. Mukherjee, D. M. Niedzwiedzki, S. Gangopadhyay and P. Biswas, *J. Am. Chem. Soc.*, 2012, **134**, 11276–11281.

52 K. Maeda, K. Teramura, D. Lu, T. Takata, N. Saito, Y. Inoue and K. Domen, *Nature*, 2006, **440**, 295.

53 X. Wang, K. Maeda, A. Thomas, K. Takanabe, G. Xin, J. M. Carlsson, K. Domen and M. Antonietti, *Nat. Mater.*, 2009, **8**, 76–80.

54 S. Kuwabata, K. Nishida, R. Tsuda, H. Inoue and H. Yoneyama, *J. Electrochem. Soc.*, 1994, **141**, 1498–1503.

55 E. E. Barton, D. M. Rampulla and A. B. Bocarsly, *J. Am. Chem. Soc.*, 2008, **130**, 6342–6344.

56 O. Ola and M. Mercedes Maroto-Valer, *Catal. Sci. Technol.*, 2014, **4**, 1631–1637.

57 L. Zhang, H. Cheng, R. Zong and Y. Zhu, *J. Phys. Chem. C*, 2009, **113**, 2368–2374.

58 P. D. Tran, S. K. Batabyal, S. S. Pramana, J. Barber, L. H. Wong and S. C. J. Loo, *Nanoscale*, 2012, **4**, 3875–3878.

59 R. J. Braham and A. T. Harris, *Ind. Eng. Chem. Res.*, 2009, **48**, 8890–8905.

60 Z. Xing, X. Zong, J. Pan and L. Wang, *Chem. Eng. Sci.*, 2013, **104**, 125–146.

61 I. Rossetti, A. Villa, C. Pirola, L. Prati and G. Ramis, *RSC Adv.*, 2014, **4**, 28883–28885.

62 M. D. Doherty, D. C. Grills, J. T. Muckerman, D. E. Polyansky and E. Fujita, *Coord. Chem. Rev.*, 2010, **254**, 2472–2482.

63 W. Tu, Y. Zhou and Z. Zou, *Adv. Mater.*, 2014, **26**, 4607–4626.

64 H. Huang, S. Wang, Y. Zhang and P. K. Chu, *RSC Adv.*, 2014, **4**, 41219–41227.

65 G. Xi, S. Ouyang, P. Li, J. Ye, Q. Ma, N. Su, H. Bai and C. Wang, *Angew. Chem.*, 2012, **124**, 2445–2449.

66 A. M. Smith and S. Nie, *Acc. Chem. Res.*, 2009, **43**, 190–200.

67 Y. Liao, S.-W. Cao, Y. Yuan, Q. Gu, Z. Zhang and C. Xue, *Chem.–Eur. J.*, 2014, **20**, 10220–10222.

68 T. Yui, A. Kan, C. Saitoh, K. Koike, T. Ibusuki and O. Ishitani, *ACS Appl. Mater. Interfaces*, 2011, **3**, 2594–2600.

69 G. Liu, J. C. Yu, G. Q. Lu and H.-M. Cheng, *Chem. Commun.*, 2011, **47**, 6763–6783.

70 W. Fan, Q. Zhang and Y. Wang, *Phys. Chem. Chem. Phys.*, 2013, **15**, 2632–2649.

71 Y. Izumi, *Coord. Chem. Rev.*, 2013, **257**, 171–186.

72 C.-C. Yang, Y.-H. Yu, B. van der Linden, J. C. S. Wu and G. Mul, *J. Am. Chem. Soc.*, 2010, **132**, 8398–8406.

73 K. Sayama and H. Arakawa, *J. Phys. Chem.*, 1993, **97**, 531–533.

74 K. Li, A. D. Handoko, M. Khraisheh and J. Tang, *Nanoscale*, 2014, **6**, 9767–9773.

75 K. Iizuka, T. Wato, Y. Miseki, K. Saito and A. Kudo, *J. Am. Chem. Soc.*, 2011, **133**, 20863–20868.

76 A. Selloni, *Nat. Mater.*, 2008, **7**, 613–615.

77 Y. Liu, B. Huang, Y. Dai, X. Zhang, X. Qin, M. Jiang and M.-H. Whangbo, *Catal. Commun.*, 2009, **11**, 210–213.

78 P. Li, S. Ouyang, Y. Zhang, T. Kako and J. Ye, *J. Mater. Chem. A*, 2013, **1**, 1185–1191.

79 Q. D. Truong, T. H. Le, J. Y. Liu, C. C. Chung and Y. C. Ling, *Appl. Catal., A*, 2012, **437**, 28–35.

14512 | *J. Mater. Chem. A*, 2015, **3**, 14487–14516

This journal is © The Royal Society of Chemistry 2015

80 L. Liu, H. Zhao, J. M. Andino and Y. Li, *ACS Catal.*, 2012, **2**, 1817–1828.

81 H. G. Yang, C. H. Sun, S. Z. Qiao, J. Zou, G. Liu, S. C. Smith, H. M. Cheng and G. Q. Lu, *Nature*, 2008, **453**, 638–641.

82 M. Lazzeri, A. Vittadini and A. Selloni, *Phys. Rev. B: Condens. Matter Mater. Phys.*, 2001, **63**, 155409.

83 M. Lazzeri, A. Vittadini and A. Selloni, *Phys. Rev. B: Condens. Matter Mater. Phys.*, 2002, **65**, 119901.

84 X.-Q. Gong and A. Selloni, *J. Phys. Chem. B*, 2005, **109**, 19560–19562.

85 A. Vittadini, A. Selloni, F. P. Rotzinger and M. Grätzel, *Phys. Rev. Lett.*, 1998, **81**, 2954–2957.

86 J. Yu, J. Low, W. Xiao, P. Zhou and M. Jaroniec, *J. Am. Chem. Soc.*, 2014, **136**, 8839–8842.

87 G. Liu, H. G. Yang, X. Wang, L. Cheng, J. Pan, G. Q. Lu and H.-M. Cheng, *J. Am. Chem. Soc.*, 2009, **131**, 12868–12869.

88 J. Yu, L. Qi and M. Jaroniec, *J. Phys. Chem. C*, 2010, **114**, 13118–13125.

89 B. Wu, C. Guo, N. Zheng, Z. Xie and G. D. Stucky, *J. Am. Chem. Soc.*, 2008, **130**, 17563–17567.

90 W.-S. Wang, D.-H. Wang, W.-G. Qu, L.-Q. Lu and A.-W. Xu, *J. Phys. Chem. C*, 2012, **116**, 19893–19901.

91 D. Barpuzary, Z. Khan, N. Vinothkumar, M. De and M. Qureshi, *J. Phys. Chem. C*, 2011, **116**, 150–156.

92 V. P. Indrakanti, J. D. Kubicki and H. H. Schobert, *Energy Fuels*, 2008, **22**, 2611–2618.

93 W. Jiao, L. Wang, G. Liu, G. Q. Lu and H.-M. Cheng, *ACS Catal.*, 2012, **2**, 1854–1859.

94 Q. Liu, Y. Zhou, J. Kou, X. Chen, Z. Tian, J. Gao, S. Yan and Z. Zou, *J. Am. Chem. Soc.*, 2010, **132**, 14385–14387.

95 Q. Liu, Z.-X. Low, L. Li, A. Razmjou, K. Wang, J. Yao and H. Wang, *J. Mater. Chem. A*, 2013, **1**, 11563–11569.

96 Q. Liu, Y. Zhou, Y. Ma and Z. Zou, *RSC Adv.*, 2012, **2**, 3247–3250.

97 S. Yan, L. Wan, Z. Li and Z. Zou, *Chem. Commun.*, 2011, **47**, 5632–5634.

98 Z. Liu, X. Zhang, S. Nishimoto, M. Jin, D. A. Tryk, T. Murakami and A. Fujishima, *J. Phys. Chem. C*, 2007, **112**, 253–259.

99 M. Ye, J. Gong, Y. Lai, C. Lin and Z. Lin, *J. Am. Chem. Soc.*, 2012, **134**, 15720–15723.

100 G. K. Mor, K. Shankar, M. Paulose, O. K. Varghese and C. A. Grimes, *Nano Lett.*, 2005, **5**, 191–195.

101 S. Liang, J. He, Z. Sun, Q. Liu, Y. Jiang, H. Cheng, B. He, Z. Xie and S. Wei, *J. Phys. Chem. C*, 2012, **116**, 9049–9053.

102 K. Zhu, N. R. Neale, A. Miedaner and A. J. Frank, *Nano Lett.*, 2006, **7**, 69–74.

103 S. Rani, S. C. Roy, M. Paulose, O. K. Varghese, G. K. Mor, S. Kim, S. Yoriya, T. J. LaTempa and C. A. Grimes, *Phys. Chem. Chem. Phys.*, 2010, **12**, 2780–2800.

104 X. Chen, Y. Zhou, Q. Liu, Z. Li, J. Liu and Z. Zou, *ACS Appl. Mater. Interfaces*, 2012, **4**, 3372–3377.

105 S. Xie, Y. Wang, Q. Zhang, W. Deng and Y. Wang, *Chem. Commun.*, 2015, **51**, 3430–3433.

106 N. Zhang, S. Ouyang, T. Kako and J. Ye, *Chem. Commun.*, 2012, **48**, 1269–1271.

107 H.-A. Park, J. H. Choi, K. M. Choi, D. K. Lee and J. K. Kang, *J. Mater. Chem.*, 2012, **22**, 5304–5307.

108 W.-N. Wang, J. Park and P. Biswas, *Catal. Sci. Technol.*, 2011, **1**, 593–600.

109 N. Bao, L. Shen, T. Takata and K. Domen, *Chem. Mater.*, 2007, **20**, 110–117.

110 J. Guo, S. Ouyang, T. Kako and J. Ye, *Appl. Surf. Sci.*, 2013, **280**, 418–423.

111 S. Yan, H. Yu, N. Wang, Z. Li and Z. Zou, *Chem. Commun.*, 2012, **48**, 1048–1050.

112 J. Núñez, V. A. de la Peña O'Shea, P. Jana, J. M. Coronado and D. P. Serrano, *Catal. Today*, 2013, **209**, 21–27.

113 S. C. Yan, S. X. Ouyang, J. Gao, M. Yang, J. Y. Feng, X. X. Fan, L. J. Wan, Z. S. Li, J. H. Ye, Y. Zhou and Z. G. Zou, *Angew. Chem., Int. Ed.*, 2010, **49**, 6400–6404.

114 N. Zhang, S. Ouyang, P. Li, Y. Zhang, G. Xi, T. Kako and J. Ye, *Chem. Commun.*, 2011, **47**, 2041–2043.

115 X. Wang, K. Maeda, A. Thomas, K. Takanabe, G. Xin, J. M. Carlsson, K. Domen and M. Antonietti, *Nat. Mater.*, 2009, **8**, 76–80.

116 G. Liu, P. Niu, C. Sun, S. C. Smith, Z. Chen, G. Q. Lu and H.-M. Cheng, *J. Am. Chem. Soc.*, 2010, **132**, 11642–11648.

117 C. Pan, J. Xu, Y. Wang, D. Li and Y. Zhu, *Adv. Funct. Mater.*, 2012, **22**, 1518–1524.

118 L. Ge, F. Zuo, J. Liu, Q. Ma, C. Wang, D. Sun, L. Bartels and P. Feng, *J. Phys. Chem. C*, 2012, **116**, 13708–13714.

119 G. Dong and L. Zhang, *J. Mater. Chem.*, 2012, **22**, 1160–1166.

120 J. Mao, T. Peng, X. Zhang, K. Li, L. Ye and L. Zan, *Catal. Sci. Technol.*, 2013, **3**, 1253–1260.

121 Y. Li, W.-N. Wang, Z. Zhan, M.-H. Woo, C.-Y. Wu and P. Biswas, *Appl. Catal., B*, 2010, **100**, 386–392.

122 H.-C. Yang, H.-Y. Lin, Y.-S. Chien, J. Wu and H.-H. Wu, *Catal. Lett.*, 2009, **131**, 381–387.

123 X. Li, Z. Zhuang, W. Li and H. Pan, *Appl. Catal., A*, 2012, **429–430**, 31–38.

124 T. W. Kim, S. J. Hwang, S. H. Jhung, J. S. Chang, H. Park, W. Choi and J. H. Choy, *Adv. Mater.*, 2008, **20**, 539–542.

125 T. W. Kim, S. G. Hur, S. J. Hwang, H. Park, W. Choi and J. H. Choy, *Adv. Funct. Mater.*, 2007, **17**, 307–314.

126 J. Wu, Y. Cheng, J. Lin, Y. Huang, M. Huang and S. Hao, *J. Phys. Chem. C*, 2007, **111**, 3624–3628.

127 X. Li, N. Kikugawa and J. Ye, *Adv. Mater.*, 2008, **20**, 3816–3819.

128 X. Li, H. Pan, W. Li and Z. Zhuang, *Appl. Catal., A*, 2012, **413–414**, 103–108.

129 X. Li, W. Li, Z. Zhuang, Y. Zhong, Q. Li and L. Wang, *J. Phys. Chem. C*, 2012, **116**, 16047–16053.

130 J. Yoshimura, Y. Ebina, J. Kondo, K. Domen and A. Tanaka, *J. Phys. Chem.*, 1993, **97**, 1970–1973.

131 J. Gascon, U. Aktay, M. D. Hernandez-Alonso, G. P. M. van Klink and F. Kapteijn, *J. Catal.*, 2009, **261**, 75–87.

132 J. C. Lavalley, *Catal. Today*, 1996, **27**, 377–401.

133 M. G. Plaza, C. Pevida, A. Arenillas, F. Rubiera and J. J. Pis, *Fuel*, 2007, **86**, 2204–2212.

134 N. Ahmed, Y. Shibata, T. Taniguchi and Y. Izumi, *J. Catal.*, 2011, **279**, 123–135.

This journal is © The Royal Society of Chemistry 2015

J. Mater. Chem. A, 2015, **3**, 14487–14516 | **14513**

135 F. Sastre, A. Corma and H. Garcia, *J. Am. Chem. Soc.*, 2012, **134**, 14137–14141.

136 N. Ahmed, M. Morikawa and Y. Izumi, *Catal. Today*, 2012, **185**, 263–269.

137 C. M. A. Parlett, K. Wilson and A. F. Lee, *Chem. Soc. Rev.*, 2013, **42**, 3876–3893.

138 J. Yu, J. Fan and L. Zhao, *Electrochim. Acta*, 2010, **55**, 597–602.

139 P. L. Richardson, M. L. N. Perdigoto, W. Wang and R. J. G. Lopes, *Appl. Catal., B*, 2013, **132–133**, 408–415.

140 H. Bai, Z. Liu and D. D. Sun, *Int. J. Hydrogen Energy*, 2012, **37**, 13998–14008.

141 F. Dong, Y. Sun, M. Fu, W.-K. Ho, S. C. Lee and Z. Wu, *Langmuir*, 2011, **28**, 766–773.

142 Y. J. Hwang, C. H. Wu, C. Hahn, H. E. Jeong and P. Yang, *Nano Lett.*, 2012, **12**, 1678–1682.

143 S. H. Ko, D. Lee, H. W. Kang, K. H. Nam, J. Y. Yeo, S. J. Hong, C. P. Grigoropoulos and H. J. Sung, *Nano Lett.*, 2011, **11**, 666–671.

144 M.-S. Gui and W.-D. Zhang, *Nanotechnology*, 2011, **22**, 265601.

145 J. Hou, R. Cao, Z. Wang, S. Jiao and H. Zhu, *J. Hazard. Mater.*, 2012, **217–218**, 177–186.

146 J. Duan, W. Shi, L. Xu, G. Mou, Q. Xin and J. Guan, *Chem. Commun.*, 2012, **48**, 7301–7303.

147 J. Hou, Y. Qu, D. Krsmanovic, C. Ducati, D. Eder and R. V. Kumar, *J. Mater. Chem.*, 2010, **20**, 2418–2423.

148 J. Hou, Z. Wang, S. Jiao and H. Zhu, *J. Hazard. Mater.*, 2011, **192**, 1772–1779.

149 Z. Wang, J. Hou, C. Yang, S. Jiao, K. Huang and H. Zhu, *Phys. Chem. Chem. Phys.*, 2013, **15**, 3249–3255.

150 L. Zhou, W. Wang, H. Xu, S. Sun and M. Shang, *Chem.–Eur. J.*, 2009, **15**, 1776–1782.

151 Z. Khan, M. Khannam, N. Vinothkumar, M. De and M. Qureshi, *J. Mater. Chem.*, 2012, **22**, 12090–12095.

152 G. Xi, B. Yue, J. Cao and J. Ye, *Chem.–Eur. J.*, 2011, **17**, 5145–5154.

153 D. Chen and J. Ye, *Adv. Funct. Mater.*, 2008, **18**, 1922–1928.

154 J. Yu, W. Liu and H. Yu, *Cryst. Growth Des.*, 2008, **8**, 930–934.

155 Q. Liu, Y. Zhou, Z. Tian, X. Chen, J. Gao and Z. Zou, *J. Mater. Chem.*, 2012, **22**, 2033–2038.

156 Z. Li, Y. Zhou, J. Zhang, W. Tu, Q. Liu, T. Yu and Z. Zou, *Cryst. Growth Des.*, 2012, **12**, 1476–1481.

157 H. Cheng, B. Huang, Y. Liu, Z. Wang, X. Qin, X. Zhang and Y. Dai, *Chem. Commun.*, 2012, **48**, 9729–9731.

158 H. Zhou, J. Guo, P. Li, T. Fan, Z. Di and J. Ye, *Sci. Rep.*, 2013, **3**, 1667.

159 L. Yuliati, T. Hattori, H. Itoh and H. Yoshida, *J. Catal.*, 2008, **257**, 396–402.

160 N. Serpone, P. Maruthamuthu, P. Pichat, E. Pelizzetti and H. Hidaka, *J. Photochem. Photobiol., A*, 1995, **85**, 247–255.

161 H. Park, W. Choi and M. R. Hoffmann, *J. Mater. Chem.*, 2008, **18**, 2379–2385.

162 C. Wang, R. L. Thompson, J. Baltrus and C. Matranga, *J. Phys. Chem. Lett.*, 2009, **1**, 48–53.

163 M. Abou Asi, C. He, M. Su, D. Xia, L. Lin, H. Deng, Y. Xiong, R. Qiu and X.-z. Li, *Catal. Today*, 2011, **175**, 256–263.

164 S. Qin, F. Xin, Y. Liu, X. Yin and W. Ma, *J. Colloid Interface Sci.*, 2011, **356**, 257–261.

165 X. Li, H. Liu, D. Luo, J. Li, Y. Huang, H. Li, Y. Fang, Y. Xu and L. Zhu, *Chem. Eng. J.*, 2012, **180**, 151–158.

166 Q. D. Truong, J.-Y. Liu, C.-C. Chung and Y.-C. Ling, *Catal. Commun.*, 2012, **19**, 85–89.

167 G. Ghadimkhani, N. R. de Tacconi, W. Chanmanee, C. Janaky and K. Rajeshwar, *Chem. Commun.*, 2013, **49**, 1297–1299.

168 S.-I. In, D. D. Vaughn and R. E. Schaak, *Angew. Chem., Int. Ed.*, 2012, **51**, 3915–3918.

169 W. Wang, M. Dahl and Y. Yin, *Chem. Mater.*, 2012, **25**, 1179–1189.

170 W. Kim, T. Seok and W. Choi, *Energy Environ. Sci.*, 2012, **5**, 6066–6070.

171 W. J. Youngblood, S.-H. A. Lee, Y. Kobayashi, E. A. Hernandez-Pagan, P. G. Hoertz, T. A. Moore, A. L. Moore, D. Gust and T. E. Mallouk, *J. Am. Chem. Soc.*, 2009, **131**, 926–927.

172 R. Abe, K. Shinmei, K. Hara and B. Ohtani, *Chem. Commun.*, 2009, 3577–3579.

173 W. Kim, T. Tachikawa, T. Majima and W. Choi, *J. Phys. Chem. C*, 2009, **113**, 10603–10609.

174 Y.-J. Yuan, Z.-T. Yu, J.-Y. Zhang and Z.-G. Zou, *Dalton Trans.*, 2012, **41**, 9594–9597.

175 T. W. Woolerton, S. Sheard, E. Pierce, S. W. Ragsdale and F. A. Armstrong, *Energy Environ. Sci.*, 2011, **4**, 2393–2399.

176 T. W. Woolerton, S. Sheard, E. Reisner, E. Pierce, S. W. Ragsdale and F. A. Armstrong, *J. Am. Chem. Soc.*, 2010, **132**, 2132–2133.

177 A. Parkin, J. Seravalli, K. A. Vincent, S. W. Ragsdale and F. A. Armstrong, *J. Am. Chem. Soc.*, 2007, **129**, 10328–10329.

178 P. Trogadas, T. F. Fuller and P. Strasser, *Carbon*, 2014, **75**, 5–42.

179 E. Yli-Rantala, A. Pasanen, P. Kauranen, V. Ruiz, M. Borghei, E. Kauppinen, A. Oyarce, G. Lindbergh, C. Lagergren, M. Darab, S. Sunde, M. Thomassen, S. Ma-Andersen and E. Skou, *Fuel Cells*, 2011, **11**, 715–725.

180 Y.-P. Sun, B. Zhou, Y. Lin, W. Wang, K. A. S. Fernando, P. Pathak, M. J. Meziani, B. A. Harruff, X. Wang, H. Wang, P. G. Luo, H. Yang, M. E. Kose, B. Chen, L. M. Veca and S.-Y. Xie, *J. Am. Chem. Soc.*, 2006, **128**, 7756–7757.

181 A. B. Bourlinos, A. Stassinopoulos, D. Anglos, R. Zboril, M. Karakassides and E. P. Giannelis, *Small*, 2008, **4**, 455–458.

182 H. Peng and J. Travas-Sejdic, *Chem. Mater.*, 2009, **21**, 5563–5565.

183 H. Jiang, F. Chen, M. G. Lagally and F. S. Denes, *Langmuir*, 2009, **26**, 1991–1995.

184 L. Cao, S. Sahu, P. Anilkumar, C. E. Bunker, J. Xu, K. A. S. Fernando, P. Wang, E. A. Guliants, K. N. Tackett and Y.-P. Sun, *J. Am. Chem. Soc.*, 2011, **133**, 4754–4757.

185 W.-J. Ong, M. M. Gui, S.-P. Chai and A. R. Mohamed, *RSC Adv.*, 2013, **3**, 4505–4509.

14514 | *J. Mater. Chem. A*, 2015, **3**, 14487–14516

This journal is © The Royal Society of Chemistry 2015

186 L. Jia, D.-H. Wang, Y.-X. Huang, A.-W. Xu and H.-Q. Yu, *J. Phys. Chem. C*, 2011, **115**, 11466–11473.

187 A. K. Agegnehu, C.-J. Pan, J. Rick, J.-F. Lee, W.-N. Su and B.-J. Hwang, *J. Mater. Chem.*, 2012, **22**, 13849–13854.

188 P. Gao, J. Liu, S. Lee, T. Zhang and D. D. Sun, *J. Mater. Chem.*, 2012, **22**, 2292–2298.

189 Z. Khan, T. R. Chetia, A. K. Vardhaman, D. Barpuzary, C. V. Sastri and M. Qureshi, *RSC Adv.*, 2012, **2**, 12122–12128.

190 J. Hou, Z. Wang, W. Kan, S. Jiao, H. Zhu and R. V. Kumar, *J. Mater. Chem.*, 2012, **22**, 7291–7299.

191 F. Pei, Y. Liu, S. Xu, J. Lü, C. Wang and S. Cao, *Int. J. Hydrogen Energy*, 2013, **38**, 2670–2677.

192 T. Peng, K. Li, P. Zeng, Q. Zhang and X. Zhang, *J. Phys. Chem. C*, 2012, **116**, 22720–22726.

193 Q. Xiang, J. Yu and M. Jaroniec, *J. Am. Chem. Soc.*, 2012, **134**, 6575–6578.

194 H.-i. Kim, G.-h. Moon, D. Monllor-Satoca, Y. Park and W. Choi, *J. Phys. Chem. C*, 2011, **116**, 1535–1543.

195 N. Yang, J. Zhai, D. Wang, Y. Chen and L. Jiang, *ACS Nano*, 2010, **4**, 887–894.

196 I. V. Lightcap and P. V. Kamat, *J. Am. Chem. Soc.*, 2012, **134**, 7109–7116.

197 P. Wang, Y. Zhai, D. Wang and S. Dong, *Nanoscale*, 2011, **3**, 1640–1645.

198 Y. Zhang, Z.-R. Tang, X. Fu and Y.-J. Xu, *ACS Nano*, 2011, **5**, 7426–7435.

199 X. Pan, Y. Zhao, S. Liu, C. L. Korzeniewski, S. Wang and Z. Fan, *ACS Appl. Mater. Interfaces*, 2012, **4**, 3944–3950.

200 J. Du, X. Lai, N. Yang, J. Zhai, D. Kisailus, F. Su, D. Wang and L. Jiang, *ACS Nano*, 2010, **5**, 590–596.

201 J. Zhang, Z. Zhu, Y. Tang and X. Feng, *J. Mater. Chem.*, 2013, **1**, 3752–3756.

202 A. Peigney, C. Laurent, E. Flahaut, R. R. Bacsa and A. Rousset, *Carbon*, 2001, **39**, 507–514.

203 A. Ghosh, K. S. Subrahmanyam, K. S. Krishna, S. Datta, A. Govindaraj, S. K. Pati and C. N. R. Rao, *J. Phys. Chem. C*, 2008, **112**, 15704–15707.

204 B. Huang, Z. Li, Z. Liu, G. Zhou, S. Hao, J. Wu, B.-L. Gu and W. Duan, *J. Phys. Chem. C*, 2008, **112**, 13442–13446.

205 Y. Zhang, N. Zhang, Z.-R. Tang and Y.-J. Xu, *ACS Nano*, 2012, **6**, 9777–9789.

206 Y. T. Liang, B. K. Vijayan, K. A. Gray and M. C. Hersam, *Nano Lett.*, 2011, **11**, 2865–2870.

207 X.-J. Lv, W.-F. Fu, C.-Y. Hu, Y. Chen and W.-B. Zhou, *RSC Adv.*, 2013, **3**, 1753–1757.

208 H.-C. Hsu, I. Shown, H.-Y. Wei, Y.-C. Chang, H.-Y. Du, Y.-G. Lin, C.-A. Tseng, C.-H. Wang, L.-C. Chen, Y.-C. Lin and K.-H. Chen, *Nanoscale*, 2013, **5**, 262–268.

209 Y. T. Liang, B. K. Vijayan, O. Lyandres, K. A. Gray and M. C. Hersam, *J. Phys. Chem. Lett.*, 2012, **3**, 1760–1765.

210 W. Tu, Y. Zhou, Q. Liu, Z. Tian, J. Gao, X. Chen, H. Zhang, J. Liu and Z. Zou, *Adv. Funct. Mater.*, 2012, **22**, 1215–1221.

211 P. Pathak, S. Gupta, K. Grosulak, H. Imahori and V. Subramanian, *J. Phys. Chem. C*, 2015, **119**, 7543–7553.

212 B. Mukherjee, S. Gupta, A. Peterson, H. Imahori, A. Manivannan and V. Subramanian, *Chem.–Eur. J.*, 2014, **20**, 10456–10465.

213 A. Iwase, H. Kato and A. Kudo, *Catal. Lett.*, 2006, **108**, 7–10.

214 M. Liu, W. You, Z. Lei, G. Zhou, J. Yang, G. Wu, G. Ma, G. Luan, T. Takata, M. Hara, K. Domen and C. Li, *Chem. Commun.*, 2004, 2192–2193.

215 Y. Mizukoshi, K. Sato, T. J. Konno and N. Masahashi, *Appl. Catal., B*, 2010, **94**, 248–253.

216 M. Hara, J. Nunoshige, T. Takata, J. N. Kondo and K. Domen, *Chem. Commun.*, 2003, 3000–3001.

217 V. Subramanian, E. Wolf and P. V. Kamat, *J. Phys. Chem. B*, 2001, **105**, 11439–11446.

218 V. Subramanian, E. E. Wolf and P. V. Kamat, *J. Am. Chem. Soc.*, 2004, **126**, 4943–4950.

219 D. Kong, J. Z. Y. Tan, F. Yang, J. Zeng and X. Zhang, *Appl. Surf. Sci.*, 2013, **277**, 105–110.

220 X. Feng, J. D. Sloppy, T. J. LaTempa, M. Paulose, S. Komarneni, N. Bao and C. A. Grimes, *J. Mater. Chem.*, 2011, **21**, 13429–13433.

221 Z. W. Seh, S. Liu, M. Low, S.-Y. Zhang, Z. Liu, A. Mlayah and M.-Y. Han, *Adv. Mater.*, 2012, **24**, 2310–2314.

222 Q. Zhang, D. Q. Lima, I. Lee, F. Zaera, M. Chi and Y. Yin, *Angew. Chem.*, 2011, **123**, 7226–7230.

223 T. Takahashi, A. Kudo, S. Kuwabata, A. Ishikawa, H. Ishihara, Y. Tsuboi and T. Torimoto, *J. Phys. Chem. C*, 2012, **117**, 2511–2520.

224 K. Awazu, M. Fujimaki, C. Rockstuhl, J. Tominaga, H. Murakami, Y. Ohki, N. Yoshida and T. Watanabe, *J. Am. Chem. Soc.*, 2008, **130**, 1676–1680.

225 X. Zhou, G. Liu, J. Yu and W. Fan, *J. Mater. Chem.*, 2012, **22**, 21337–21354.

226 W. A. Murray and W. L. Barnes, *Adv. Mater.*, 2007, **19**, 3771–3782.

227 S. Linic, P. Christopher and D. B. Ingram, *Nat. Mater.*, 2011, **10**, 911–921.

228 H. Zhu, X. Chen, Z. Zheng, X. Ke, E. Jaatinen, J. Zhao, C. Guo, T. Xie and D. Wang, *Chem. Commun.*, 2009, 7524–7526.

229 X. Zhang, PhD thesis, Queensland University of Technology, 2014, http://eprints.qut.edu.au/67714/ (accessed June 2nd, 2015).

230 M. S. Shore, J. Wang, A. C. Johnston-Peck, A. L. Oldenburg and J. B. Tracy, *Small*, 2011, **7**, 230–234.

231 P. Wang, B. Huang, Y. Dai and M.-H. Whangbo, *Phys. Chem. Chem. Phys.*, 2012, **14**, 9813–9825.

232 M. Xiao, R. Jiang, F. Wang, C. Fang, J. Wang and J. C. Yu, *J. Mater. Chem. A*, 2013, **1**, 5790–5805.

233 D. M. Bijith, J. Babu and K. G. Vinay, *Nanotechnology*, 2013, **24**, 405402.

234 Z. Zhang, Z. Wang, S.-W. Cao and C. Xue, *J. Phys. Chem. C*, 2013, **117**, 25939–25947.

235 C. An, J. Wang, W. Jiang, M. Zhang, X. Ming, S. Wang and Q. Zhang, *Nanoscale*, 2012, **4**, 5646–5650.

236 J. Z. Y. Tan, Y. Fernandez, D. Liu, M. Maroto-Valer, J. Bian and X. Zhang, *Chem. Phys. Lett.*, 2012, **531**, 149–154.

237 J.-J. Chen, J. C. S. Wu, P. C. Wu and D. P. Tsai, *J. Phys. Chem. C*, 2010, **115**, 210–216.

238 Q. Xiang, J. Yu and M. Jaroniec, *Phys. Chem. Chem. Phys.*, 2011, **13**, 4853–4861.

239 K. Iwashina and A. Kudo, *J. Am. Chem. Soc.*, 2011, **133**, 13272–13275.

240 F. Dong, S. Guo, H. Wang, X. Li and Z. Wu, *J. Phys. Chem. C*, 2011, **115**, 13285–13292.

241 S. Bingham and W. A. Daoud, *J. Mater. Chem.*, 2011, **21**, 2041–2050.

242 J. Zhang, Y. Wu, M. Xing, S. A. K. Leghari and S. Sajjad, *Energy Environ. Sci.*, 2010, **3**, 715–726.

243 C.-W. Tsai, H. M. Chen, R.-S. Liu, K. Asakura and T.-S. Chan, *J. Phys. Chem. C*, 2011, **115**, 10180–10186.

244 I. Tsuji, H. Kato and A. Kudo, *Angew. Chem., Int. Ed.*, 2005, **44**, 3565–3568.

245 I. Tsuji, H. Kato, H. Kobayashi and A. Kudo, *J. Am. Chem. Soc.*, 2004, **126**, 13406–13413.

246 K. Maeda and K. Domen, *Chem. Mater.*, 2009, **22**, 612–623.

247 K. Maeda, T. Takata, M. Hara, N. Saito, Y. Inoue, H. Kobayashi and K. Domen, *J. Am. Chem. Soc.*, 2005, **127**, 8286–8287.

248 J.-Y. Liu, B. Garg and Y.-C. Ling, *Green Chem.*, 2011, **13**, 2029–2031.

249 Q. Zhai, S. Xie, W. Fan, Q. Zhang, Y. Wang, W. Deng and Y. Wang, *Angew. Chem., Int. Ed.*, 2013, **52**, 5776–5779.

250 P. Li, H. Xu, L. Liu, T. Kako, N. Umezawa, H. Abe and J. Ye, *J. Mater. Chem. A*, 2014, **2**, 5606–5609.

251 P. Christopher, H. Xin and S. Linic, *Nat. Chem.*, 2011, **3**, 467–472.

252 H. Zhu, X. Ke, X. Yang, S. Sarina and H. Liu, *Angew. Chem., Int. Ed.*, 2010, **49**, 9657–9661.

253 S. F. J. Hackett, R. M. Brydson, M. H. Gass, I. Harvey, A. D. Newman, K. Wilson and A. F. Lee, *Angew. Chem., Int. Ed.*, 2007, **46**, 8593–8596.

254 J. Xing, J. F. Chen, Y. H. Li, W. T. Yuan, Y. Zhou, L. R. Zheng, H. F. Wang, P. Hu, Y. Wang, H. J. Zhao, Y. Wang and H. G. Yang, *Chem.–Eur. J.*, 2014, **20**, 2085.

255 A. Bruix, Y. Lykhach, I. Matolínová, A. Neitzel, T. Skála, N. Tsud, M. Vorokhta, V. Stetsovych, K. Ševčíková, J. Mysliveček, R. Fiala, M. Václavů, K. C. Prince, S. Bruyère, V. Potin, F. Illas, V. Matolín, J. Libuda and K. M. Neyman, *Angew. Chem., Int. Ed.*, 2014, **53**, 10525–10530.

256 G. Pei, X. Liu, A. Wang, A. F. Lee, M. A. Isaacs, L. Li, X. Pan, X. Yang, X. Wang, Z. Tai, K. Wilson and T. Zhang, *ACS Catal.*, 2015, **5**, 3717–3725.

257 C. Pirez, K. Wilson and A. F. Lee, *Green Chem.*, 2014, **16**, 197–202.

258 P. Anastas and N. Eghbali, *Chem. Soc. Rev.*, 2010, **39**, 301–312.